Quantifying the drivers of terrestrial drought and water stress impacts on carbon uptake in China

Yuanhang Yang[1], Jiabo Yin[1*], Shengyu Kang[1], Louise J. Slater[2], Xihui Gu[3], Aliaksandr Volchak[4]

[1]State Key Laboratory of Water Resources and Management, Wuhan University, Wuhan, Hubei, 430072, P.R. China

[2]School of Geography and the Environment, University of Oxford, Oxford, UK

[3]School of Environmental Studies, China University of Geosciences, Wuhan 430074, China

[4]Engineering Systems and Ecology Faculty, Brest State Technical University, Moskovskaya 267, 224017 Brest, Belarus

*Correspondence: Jiabo Yin (jboyn@whu.edu.cn)

Highlights:

- We quantify the impacts of water stress on ecosystem carbon uptake in China.
- We explore the atmospheric driving mechanisms of droughts.
- Drought frequency is projected to increase sixfold over 60% of land by the late 21st century.
- Future water stress is likely to decrease carbon storage under climate change.

Abstract: Droughts are one of the most damaging weather-related hazards and can have detrimental impacts on ecosystem carbon uptake. However, little is known about the physical mechanisms underlying drought evolution as well as their potential effects on the carbon budget under historical and future climates. Here, we first quantify the impacts of water stress on carbon uptake under climate change in China. While heat and water stress play a crucial role in carbon uptake, the effect of ecosystem complexity is also significant. Then, we employ a machine learning model to explore the driving mechanisms of droughts, which are identified through the depletion of terrestrial water storage (TWS). Our results indicate that TWS droughts tend to be governed by atmospheric dryness, with precipitation, relative humidity (RH) and temperature playing dominant roles in drought evolution across most land areas. Precipitation and RH control moisture supply and demand, while rising temperature signifies increasing evaporative demand and enhanced evapotranspiration, leading to soil moisture depletion and reduced surface runoff, thereby intensifying drought. Further, by combining satellite data, field measurements, six global hydrological models, a global land surface model and a dynamic vegetation model, we find that water and heat stress have negative impacts on gross primary productivity (GPP), total ecosystem respiration (TER) and net ecosystem productivity (NEP), under both current and future climates. By the end of the 21st century (2071-2100), drought occurrence is projected to increase by sixfold over more than 60% of land areas, leading to disproportionate negative impacts on carbon assimilation. Negative anomalies of NEP under drought stress are projected to decline from -0.09 $g \cdot m^{-2} \cdot day^{-1}$ (historical period) to -0.16 $g \cdot m^{-2} \cdot day^{-1}$ (future period) under SSP370, with even more severe effects on future carbon assimilation under higher emission pathways. Our results suggest that more severe drought conditions might challenge ecosystem sustainability, and highlight the necessity of improving ecosystem resilience to climate warming.

Key words: water stress, carbon uptake, drought, machine learning, China

1. Introduction

The rapid development of human activities since the industrial revolution has contributed to increasing emissions of greenhouse gases, altering the Earth's water and carbon cycles (Yin et al., 2018; Gao et al., 2021; Good et al., 2021). The terrestrial biosphere, a prominent carbon sink, absorbs about 30 percent of anthropogenic carbon dioxide (CO_2) emissions (Green et al., 2019; Friedlingstein et al., 2022). However, water stress has a significant impact on the exchanges of carbon and water between land and atmosphere, and may alter carbon uptake due to seasonal climatic changes and long-term shifts in ecosystem succession (Gentine et al., 2019; El-Madany et al., 2020; Xu et al., 2020; Zhang et al., 2020). For example, soil moisture content determines water availability for plant roots and regulates stomatal conductance, thereby influencing the rates of gross primary productivity (GPP) and total ecosystem respiration (TER). Water stress from drying soil moisture can reduce GPP and TER through both stomatal and non-stomatal mechanisms, as well as through soil enzyme activities impacting microbial respiration. This can lead to vegetation mortality and further exacerbate climate extremes through land-atmosphere coupling effects (Schwalm et al., 2017; Humphrey et al., 2018).

Numerous studies have reported that climate warming is increasingly constraining the terrestrial carbon sink. As climate changes, more frequent and persistent weather-related hazards, such as droughts, are leading to economic, societal, and environmental challenges across the globe (Sui et al., 2018; Gu et al., 2020; Ogunrinde et al., 2023). Recently, droughts have received more attention due to their complex effects on ecosystem productivity. For example, the 2018 European summer drought and the 2015-2016 Amazon drought both revealed that drought is one of the most significant stressors of carbon assimilation at regional and global scales (Zscheischler et al., 2014; Ruehr et al., 2019). Some studies have attempted to quantify how vegetation greenness and the carbon budget respond to droughts, and found that droughts often coincide with heatwaves, amplifying their impacts on ecosystem productivity (Dannenberg et al., 2022; Deng et al., 2023; Yin et al., 2023a). More recently, it has been shown that GPP and net ecosystem productivity (NEP) are more sensitive to meteorological droughts than to heat stress (Deng et al., 2021; Li et al., 2021). In particular, drought is one of the most significant factors regulating vegetation greenness through its effect on both productivity and respiration, which in turn can alter the carbon cycle processes and has a feedback effect on the global climate (Chen et al., 2020). Although some plants can acclimate to climate change by minimizing the impact of heat stress on photosynthesis and lowering dark respiration rates, this acclimation potential could be overwhelmed by more severe drought events (Teskey et al., 2015; Brodribb et al., 2020). After a severe drought, plant recovery is usually delayed by slowed growth, irreversible reductions in hydraulic conductivity, or depletion of carbon stocks (Hammond et al., 2022; McDowell et al., 2022). Therefore, a better understanding of the relationship between drought and terrestrial carbon uptake is critical for exploring future climate-carbon feedbacks.

However, the appropriate approach to characterize droughts remains unresolved, particularly in terms of defining a fully representative stress index. Previous studies have assessed droughts through a variety of indices such as the Standardized Precipitation Evapotranspiration Index (SPEI), Palmer drought severity index (PDSI) and the soil moisture (SM) drought index (Zhang et al., 2021; Fu et al., 2022; Hussain et al., 2022; Xi and Yuan, 2022). These indices mainly consider one or several meteorological or hydrological variables (e.g., precipitation, evapotranspiration, runoff and SM), which only partially capture water storages or fluxes. In contrast, TWS is defined as all forms of water stored above and underneath the surface of the Earth (i.e., the sum of continental water stored in canopies, snow and ice, rivers, lakes and reservoirs, wetlands, soil and groundwater) (Syed et al., 2008; Rodell et al., 2018; Pokhrel et al., 2021). Meanwhile, it has recently been shown that terrestrial water storage (TWS), a key determinant of global water and energy budgets representing vertically integrated water storage, has large-scale impacts on hydrologic systems and vegetation growth (Rodell et al., 2018; Jing et al., 2020; Zhao et al., 2021). With the emergence of satellite remote sensing, the Gravity Recovery and Climate Experiment (GRACE) satellite and its successor (GRACE-FO) provide a versatile tool for monitoring TWS at wider coverage than before, and can effectively capture changes in water fluxes at a large scale (Sinha et al., 2019; Satish Kumar et al., 2021). Moreover, The TWS derived from GRACE data can effectively reflect the gravity changes caused by snow and ice (e.g., solid water stored in glaciers and permafrost), surface water, soil water, groundwater and human factors (Yin et al., 2022a, 2023b). Although the GRACE/GRACE-FO satellites have been applied for drought monitoring and assessment, drought projection based on TWS is still in its infancy. Furthermore, the underlying physical mechanisms behind drought evolution and their potential effects on terrestrial carbon uptake remain unclear.

In this study, the driving mechanisms of droughts and their effects on terrestrial carbon uptake are systematically investigated in China, under both historical and future periods. The objectives of this study are (1) to explore the driving mechanisms of drought characteristics under climate change by using machine learning and atmospheric dynamics; (2) to explore the effects of droughts on the carbon sink by combining data from satellites, field measurements, climate models, land surface models, global hydrological models and dynamic vegetation models. This paper provides mechanistic evidence of the impacts of climate change on water stress and its effects on the carbon sink in China.

2. Materials and methods

2.1 Measurements from eddy-covariance flux towers and in situ meteorological stations

The landscapes of China are usually divided into six types (e.g., construction land, desert, forest, grassland, shrubs, and cropland) (Zhao et al., 2020). Cropland constitutes about 23.36 %, while forest and grasslands account for 17.97 % and 23.97 % of the national land area, respectively (Wan et al., 2018). In order to fully employ the eddy-covariance flux data, we mainly focus on four land cover types, namely evergreen broadleaf forest (EBF), mixed forest (MF), grasslands (GRA), and croplands (CRO). To explore droughts and their effects on carbon uptake at a larger spatial scale, we further divide mainland China into eight geographical regions (Fig.1).

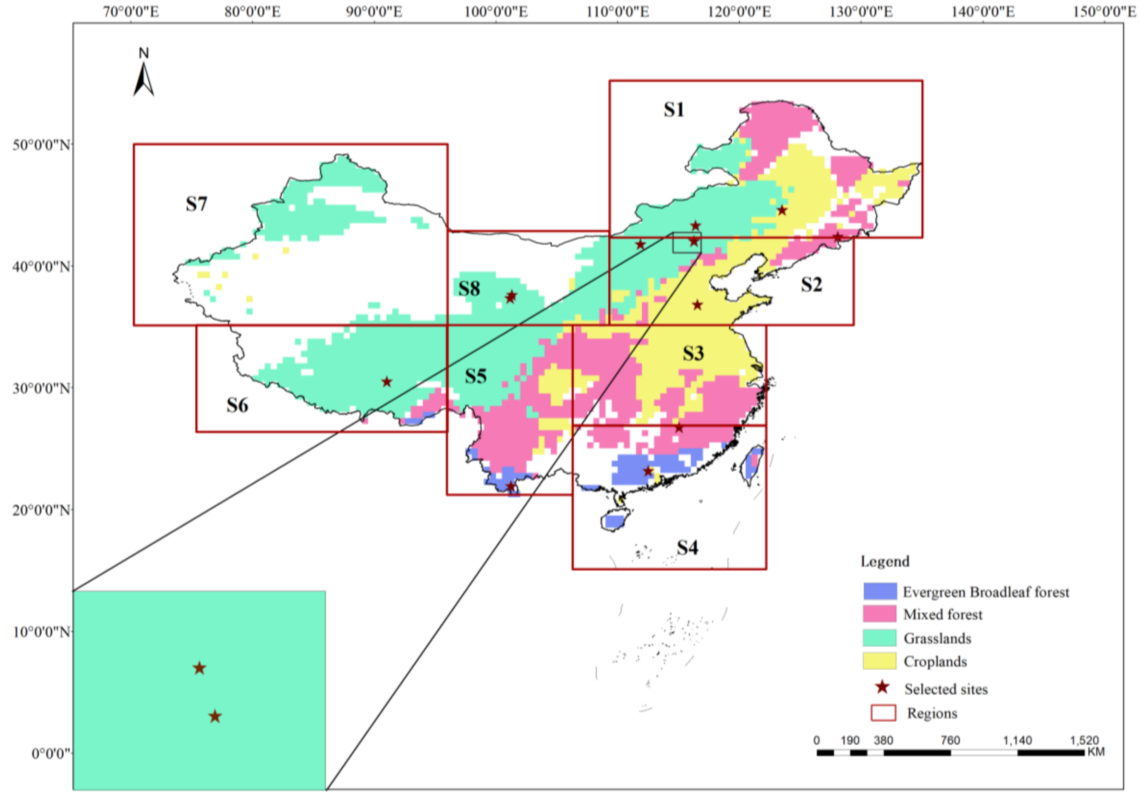

Fig. 1. Land cover types and our selected 13 flux tower sites in China. S1-Northeast China, S2-North China, S3-Jiang-Huai Region, S4-South China, S5-Southwest China, S6- Tibetan Plateau, S7-Western of Northwest China, and S8-Eastern of Northwest China.

In this study, the carbon and water fluxes and meteorology data come from the FLUXNET dataset (https://fluxnet.org/data/fluxnet2015-dataset/) and The Chinese Terrestrial Ecosystem Flux Research Network (ChinaFLUX) (http://www.china flux.org/enn/index.aspx), and we select 13 flux tower sites (i.e., all of the available sites) in China (Table S1). These sites are in different latitude zones and climatic zones, which represent different temperature and moisture gradients in the Chinese regions (Chang et al., 2023). The FLUXNET2015 dataset provides ecosystem-scale data on CO_2, water, and energy exchange between the biosphere and the atmosphere, for 212 sites around the globe (Chu et al., 2017). To evaluate the processes of ecosystem moisture and carbon exchange, we use half-hourly air temperature (T_{air}), SM, GPP, NEP and TER data from the FLUXNET2015 dataset, where TER includes both autotrophic respiration and heterotrophic respiration. These data are processed following a consistent and uniform processing pipeline (Reichstein et al., 2005). Here, the GPP is derived from the night-time partitioning method, then NEP is obtained by subtracting TER from GPP (Pastorello et al., 2020). The warm season is defined as days when the running 7-day mean temperatures are higher than the 60th percentile of the daily temperatures at each site (Yin et al., 2021). The ChinaFLUX is a long-term national network of micrometeorological flux measurement sites that measure the net exchange of carbon dioxide, water and energy between the biosphere and atmosphere, which relies on the Chinese Ecosystem Research Network (CERN), contributes to increasing the number of ecosystem types in FLUXNET (Yu et al., 2006).

Satellite-retrieved solar-induced fluorescence (SIF) has shown substantial potential for the monitoring of plant photosynthesis, which is strongly related to the spatiotemporal variation of GPP (Zhang et al., 2017, 2018). Here, we use the clear-sky daily SIF from 2000-2020 with a four-day temporal resolution and a 0.5° spatial resolution, which is generated by a machine learning algorithm based on Orbiting Carbon Observatory-2 (OCO-2) SIF observations and surface reflectance from the Moderate Resolution Imaging Spectroradiometer (MODIS) (Zhang et al., 2018). We also use a retrieved GPP dataset, which is based on an improved light use efficiency theory by assimilating satellite data from MODIS and climate data from the National Centers for Environmental Prediction (NCEP) Reanalysis II. The GPP dataset has moderate spatial (500 m) and temporal (8 days) resolution at the global scale during 2000-2019 (Zhang et al., 2017). In this study, we focus on the GPP and SIF in the warm season (i.e., five continuous months with the highest temperature) in Section 3.1 to investigate the effects of drought stress on the ecosystem carbon budget (Yang et al., 2023; Yin et al., 2023) (Fig. S1).

To provide a robust analysis of atmospheric thermodynamic and dynamic characteristics under dry conditions, we also use monthly data of precipitation, 2 m air temperature (T_{2m}), relative humidity (RH) and Convective available potential energy (CAPE) during 1979-2020 from the 20th-century reanalysis (20CR), which are used in section 3.1. The 20CR are constrained only by surface pressure, sea ice and ocean surface temperature observations. The observations of 20CR are considered to capture the climate in China well (Zhao et al., 2020; Yang et al., 2022). Moreover, 20CR provides the estimations of global tropospheric variability, and of the dataset's time-varying quality from 1871 to the present, with a temporal resolution of 6-hourly and a spatial resolution of 2°×2° (Compo et al., 2011; Laloyaux et al., 2018; Slivinski et al., 2019; Emanuel, 2021). To account for possible uncertainties caused by different data products, these datasets are interpolated to 0.5°×0.5° grids.

2.2 GRACE/GRACE-FO data and ERA5 reanalysis dataset

Here, we use TWS anomalies (TWSA) from the GRACE/GRACE-FO satellites to characterize terrestrial droughts during 2002-2021 in China. The latest mascon products are collected from three processing centres: the Jet Propulsion Laboratory of the California Institute of Technology (Landerer et al., 2020), the Center for Space Research at the University of Texas at Austin (Save et al., 2016) and the National Aeronautics and Space Administration’s Goddard Space Flight Center (Loomis et al., 2019), respectively. Considering the potential uncertainty associated with different processing procedures, we derive a multi-model ensemble mean time series of the three mascon GRACE/GRACE-FO datasets. The long-term TWSA series are derived as the anomalies of equivalent water height relative to the 2004-2009 time-mean baseline (Landerer and Swenson, 2012). Linear interpolation is employed to fill in the missing data of these products (Yin et al., 2022a). Afterwards, the average monthly TWSA time series of these products is processed for the period 2002-2021 over China.

The ERA5 reanalysis dataset produced by the European Centre for Medium Range

Weather Forecasts (ECMWF) provides real-time global hourly records from 1979 to the present at 0.25°×0.25° spatial resolution (Simmons et al., 1999). In this study, we use 12 monthly climate variables: surface sensible heat flux, latent heat flux, precipitation, air pressure (ps), snowfall, T_{2m}, dew-point temperature (T_{dew}), surface downwelling longwave radiation (rlds) and surface downwelling shortwave radiation (rsds), convective inhibition, moisture flux convergence and wind speed. With these climate variables, we first calculate the saturated water vapor pressure (e_{sat}) using the Clausius-Clapeyron (C-C) relationship method (Koutsoyiannis, 2012):

$$e_{sat}(T) = e_{s0} \exp\left[\frac{L_v}{R_v}\left(\frac{1}{T_0} - \frac{1}{T}\right)\right] \quad (1)$$

where T_0 and e_{s0} are the integration constants, taken as 273.16 K and 611 Pa, respectively; L_v is the latent heat of vaporization, taken as 2.5×10^{6} J kg^{-1}; and R_v is the water vapor gas constant, taken as 461 J kg^{-1} K^{-1}.

Then, the RH is deduced based on T_{2m} and T_{dew}: $RH = e_{sat}(T_{\mathrm{dew}}) / e_{sat}(T_{\mathrm{2m}})$. Specific humidity ($q$) is the ratio of the mass of water vapor to the total mass of the air mass, which is deduced by using ERA5 near-ground pressure and T_{dew} (Simmons et al., 1999):

$$q = 0.622\frac{e_{sat}(T_{\mathrm{dew}})}{ps - 0.378 e_{sat}(T_{\mathrm{dew}})} \quad (2)$$

2.3 Climate scenarios and carbon flux simulations under CMIP5/6

We use bias-corrected outputs from the Coupled Model Inter-comparison Project phase 6 (CMIP6) under three SSPs (SSP126, SSP370 and SSP585), which includes five global climate models (GCMs): GFDL-ESM4, IPSL-CM6ALR, MRI-ESM1-2HR, MRI-ESM2-0 and UKESM1-0-LL (Table S2). The climate model outputs have been systematically bias-corrected under the Inter-Sectoral Impact Model Inter-comparison Project (ISIMIP3b). The ISIMIP3b protocol uses a state-of-the-art statistical downscaling method to correct CMIP6 outputs towards a merged observational dataset, version 2.0 of WFDE5, over the global land surface (Fan et al., 2021; Lange et al., 2021). The TWS series of 15 members (i.e., outputs from five CMIP6 GCMs under three SSPs) are simulated by driving the H08 model (i.e., a popular global hydrological model). The H08 model simulates the water cycle globally and comprises six sub-models: land-surface hydrology, river routing, crop growth, reservoir operation, water abstraction, and environmental flow (Yoshida et al., 2022). We also use the GPP, TER and NEP outputs of these GCMs under the three SSPs, and employ data from historical (1985-2014) and future (2071-2100) periods to assess climate change impacts on the water-carbon cycle.

To evaluate the robustness of our results, the CMIP5-based TWS projections are compared with the results of CMIP6. The CMIP5-based projections include 96 scenario-model combinations, which consist of three representative concentration pathways (RCP 2.6, RCP 6.0 and RCP 8.5), four GCMs (MRI-ESM2-0、IPSL-CM6A-LR、GFDL-ESM4、HADGEM2-ES) and eight terrestrial hydrological models (THMs) (Table S3). The eight THMs include six global hydrological models (CWatM, H08, MPI-HM, PCR-GLOBWB, WaterGAP2 and WaterGAP2-2c), one global land surface model (CLM4.5) and one dynamic global vegetation model (LPJmL). All models simulate the critical terrestrial hydrological processes, and are forced by the ISIMIP2b daily meteorological forcing data from four GCMs under CMIP5 (Pachauri et al., 2014; Oh et al., 2023). In each grid cell, we define the growing season during the historical period. To evaluate the projected impacts of drought events on ecosystem carbon storage, we also use the GPP, autotrophic respiration and heterotrophic respiration outputs from the CLM4.5 model under RCP2.6 and RCP6.0, which is derived from bias-corrected GFDL-ESM2M outputs. We sum autotrophic and heterotrophic respiration to calculate TER, and then we subtract TER from GPP to obtain the NEP.

2.4 Drought identification based on TWSA-DSI

The TWSA-drought severity index (TWSA-DSI) is used to measure terrestrial dry/wet conditions (Zhao et al., 2017). A negative (positive) TWSA-DSI indicates that the TWSA is lower (higher) than the average level during the study period, and can be used to measure drought (wet) degrees, from “anomalously wet” to “very severe drought” conditions (Table S4). The TWSA-DSI is calculated as follows:

$$TWSA-DSI_{i,j} = (TWSA_{i,j} - \overline{TWSA_j}) / \sigma_j \tag{3}$$

where $TWSA_{i,j}$ represents the *TWSA* at year *i* and month *j*, $\overline{TWSA_j}$ and σ_j denote the mean value at month j and standard deviation of *TWSA* at month j, respectively.

After calculating the TWSA-DSI, we extract the drought duration, intensity, and severity by using run theory. Run theory is a useful and objective method for drought identification, where a run represents a subset of time series in which TWSA-DSI is either beneath (i.e., negative run) or over (i.e., positive run) a fixed threshold (Yevjevich, 1969). Here, a drought event is identified when TWSA-DSI is below -0.8.

2.5 Sensitivity analysis of TWSA-DSI to climate variables based on machine learning

After investigating the changes in atmospheric thermodynamic and dynamic patterns under terrestrial drought conditions, the Random Forest (RF) model is further used to disentangle the driving mechanisms of droughts by quantifying the sensitivity of TWSA-DSI to dependent climate variables. The RF model is composed of multiple regression trees. It utilizes bootstrapped samples and grows individual trees on each sample (Gu et al., 2023; Konapala and Mishra, 2020). First, we construct a random forest model in each grid to link monthly TWSA and ten meteorological variables (i.e., *precipitation, snowfall, ps, specific humidity, RH, rlds, rsds,* T_{2m}, T_{dew}, *and windspeed*). Then, each meteorological variable’s contribution to TWSA-DSI is quantified in the observation period (2002-2021), historical (1985-2014) and future (2071-2100) periods. Here, the RF is built with 500 regression trees. For each of the 500 trained trees in the random forest, assuming that perturbing one variable does not change the value of the other variables, we perturb one of the variables by 1 standard deviation (SD), and then predict TWSA-DSI using the same RF model with other same variables, including the perturbed variable. The contribution of each variable can then be estimated based on the percent of variability in TWSA-DSI from each variable (Green et al., 2020). The MATLAB function ’TreeBagger’ is used to implement the RF-based analysis (Breiman, 2001). A higher variability indicates that the target variable is more sensitive to the dependent variable. In this way, we can identify which factors contribute most to changes in the TWSA-DSI values and obtain corresponding importance ratings. The percent of the variability in TWSA-DSI is calculated as follows:

$$S_c = \frac{mean(TWSADSI_{RFc+1SD} - TWSADSI_{RFall\,\mathrm{var}})}{stdev(TWSADSI_{obs})} \times 100\% \tag{4}$$

where S_c represents the sensitivity of each climate variable to TWSA-DSI; $TWSADSI_{RFc+1SD}$ and $TWSADSI_{RFall\,\mathrm{var}}$ refer to the simulated TWSA-DSI with the perturbation of one climate variable, and the simulated TWSA-DSI with the unperturbed model, respectively; $TWSADSI_{obs}$ indicates the primary TWSA-DSI series used in training the RF model, which denotes GRACE/GRACE-FO data (in the observation period) or CMIP5/6-based simulations (during the historical or future period).

2.6 Data pre-processing and uncertainty analysis

To investigate the sensitivity and correlation between carbon and water fluxes in terrestrial ecosystems, we quantify the anomalies of GPP, TER, NEP, temperature, SM and TWSA in four land cover types (i.e., EBF, GRA, MF, CRO) using the FLUXNET dataset. First, the daily time series of all variables are detrended to remove any periodic effects during the study period. To mitigate the misleading effects of any changes in variables or differences across terrestrial ecosystems, we compute linear regression lines for each variable at every site. The detrended variables are then derived by subtracting these linear fits from the original time steps. Then, anomalies are identified by calculating the difference between a given daily value and the multi-day average of each factor. Here, the 15-day moving average of the daily data is used to represent the multi-day average, and then the corresponding values of each day are subtracted from the moving average to estimate the anomalies (Li et al., 2021).

After the detrended anomaly analysis, the daily anomalies of environmental variables (i.e., T_{air}, SM, TWSA) and carbon fluxes (i.e., GPP, TER, NEP) are pooled together for each 15-day period to perform the sensitivity analysis. The correlations between each pair of environmental variables and carbon fluxes within each of the 15-day moving windows are analyzed by using linear regression. The detrended anomalies of the carbon fluxes are the response variables, and the detrended anomalies of the environmental variables are the independent variables. The coefficients of the linear regressions between detrended anomalies of carbon fluxes and environmental variables are used to represent their sensitivity to heat and water. For example, the units of the sensitivity indices of carbon flux to air temperature and SM or TWSA are $g\ C\ m^{-2} day^{-1} {}^{\circ}C^{-1}$ and $g\ C\ m^{-2} day^{-1} mm^{-1}$, respectively. Heat stress is indicated by increasing T_{air} values, and water stress is indicated by decreasing SM or TWSA values. In other words, negative (positive) values of T_{air} (SM or TWSA) sensitivity indicate that heat and water stress significantly reduce carbon fluxes.

To project future droughts and their impacts on the carbon sink, we implement 96 scenario-model combinations from CMIP5 (i.e., three RCPs, four GCMs and eight THMs) and 15 combinations from CMIP6 (i.e., three SSPs and five GCMs). The overall uncertainty is estimated by the variance of the future projection and is then decomposed into the contributions from different sources using Analysis of variance (ANOVA). The equation is shown as follows (Yin et al., 2022b):

$$U_T = U_S + U_{GCM} + (U_{THM}) + U_{interactions} \tag{5}$$

$$U_T = \sum_{i=1}^{I}\sum_{j=1}^{J}\sum_{k=1}^{K}(Y^{i,j,k} - \overline{Y^{0,0,0}})^2 \tag{6}$$

$$U_S = J \times K \times \sum_{i=1}^{I} (Y^{i,0,0} - \overline{Y^{0,0,0}})^2 \tag{7}$$

$$U_{GCM} = I \times K \times \sum_{j=1}^{J} (Y^{0,j,0} - \overline{Y^{0,0,0}})^2 \tag{8}$$

$$U_{THM} = I \times J \times \sum_{k=1}^{K} (Y^{0,0,k} - \overline{Y^{0,0,0}})^2 \tag{9}$$

$$U_{Interactions} = \sum_{i=1}^{I} \sum_{j=1}^{J} \sum_{j=1}^{J} (Y^{i,j,k} - Y^{i,0,0} - Y^{0,j,0} - Y^{0,0,k} + 2 \times \overline{Y^{0,0,0}}) \tag{10}$$

where U_T refers to the total variance, U_S, U_{GCM}, U_{THM} and $U_{interactions}$ refer to the variance of the emission scenarios (SSP or RCP), GCMs, THMs and their interactions, respectively. I, J, K refer to the number of datasets of the emission scenarios, GCMs and THMs, respectively. $Y^{i,j,k}$ is the data source from the *i*-th emission scenarios, the *j*-th GCM and the *k*-th THM, $\overline{Y^{0,0,0}}$ represents the average of all datasets; $Y^{i,0,0}$, $Y^{0,j,0}$ and $Y^{0,0,k}$ refer to the *i*-th emission scenarios, the *j*-th GCM and the *k*-th model combination conditional data source, respectively.

3. Results

3.1 Atmospheric thermodynamic and dynamic characteristics under dry conditions

To explore the changes in atmosphere thermodynamic and dynamic patterns under terrestrial drought conditions, the TWSA-DSI is derived using the TWSA data from three GRACE/GRACE-FO mascon solutions from 2002-2021, and the thresholds of ± 0.8 are used to define dry/wet conditions. Then, we calculate the average differences of climate variables under drought conditions and under wet conditions, including sensible heat flux, latent heat flux, temperature, precipitation, specific humidity, RH, CAPE, convective inhibition, moisture flux convergence, SIF, GPP and wind speed (i.e., updraft velocity) (Fig. 2). The sensible heat flux transmitted from the land to the atmosphere strengthens when the land is dry in northeastern and southeastern China, while it weakens in northwestern China (Fig. 2a). Moreover, the pattern of anomalies of sensible heat flux is similar to that of temperature (Fig. 2c), which implies an enhancement of heat transport between land and atmosphere. The land serves as the main heat source under dry conditions across most of China, and the RH decreases (Fig. 2f) in most areas with rising temperature. Meanwhile, as evapotranspiration is limited by soil moisture and canopy water, the released latent heat cannot increase significantly; in some areas, the latent heat in dry conditions is even lower than in wet conditions (Fig. 2b). Although the atmospheric water vapor holding capacity would increase due to land warming under dry conditions, upward air flux is weakened (Fig. 2l), and therefore the atmospheric water vapor transport is limited by the sinking airflow, especially in the lower atmospheric layer. These impacts lead to spatial heterogeneity of specific humidity (Fig. 2e).

Furthermore, high values of CAPE suggest a high moist convection potential, enhancing the likelihood of intense rainstorms. CAPE is significantly lower under dry conditions than wet conditions in most areas such as southeastern and central China, while convective inhibition is relatively stronger under drought conditions in these areas (Fig. 2g-i, l). Although in some areas such as northeastern and northwestern China, CAPE is relatively stronger and CIN is lower, the intensity of changes is not significant, which means atmospheric moisture transport has weakened across almost the entire landmass, highlighting the low likelihood of convective movement generation and development. Therefore, precipitation is significantly weakened under dry conditions across large areas of China, especially in northeastern and southeastern China (Fig. 2d). Overall, atmospheric dryness usually accompanies terrestrial droughts, emphasizing the occurrence of compounding hazards due to land-atmospheric coupling and decreasing moisture supply (Zhou et al., 2019b; Yin et al., 2023a).

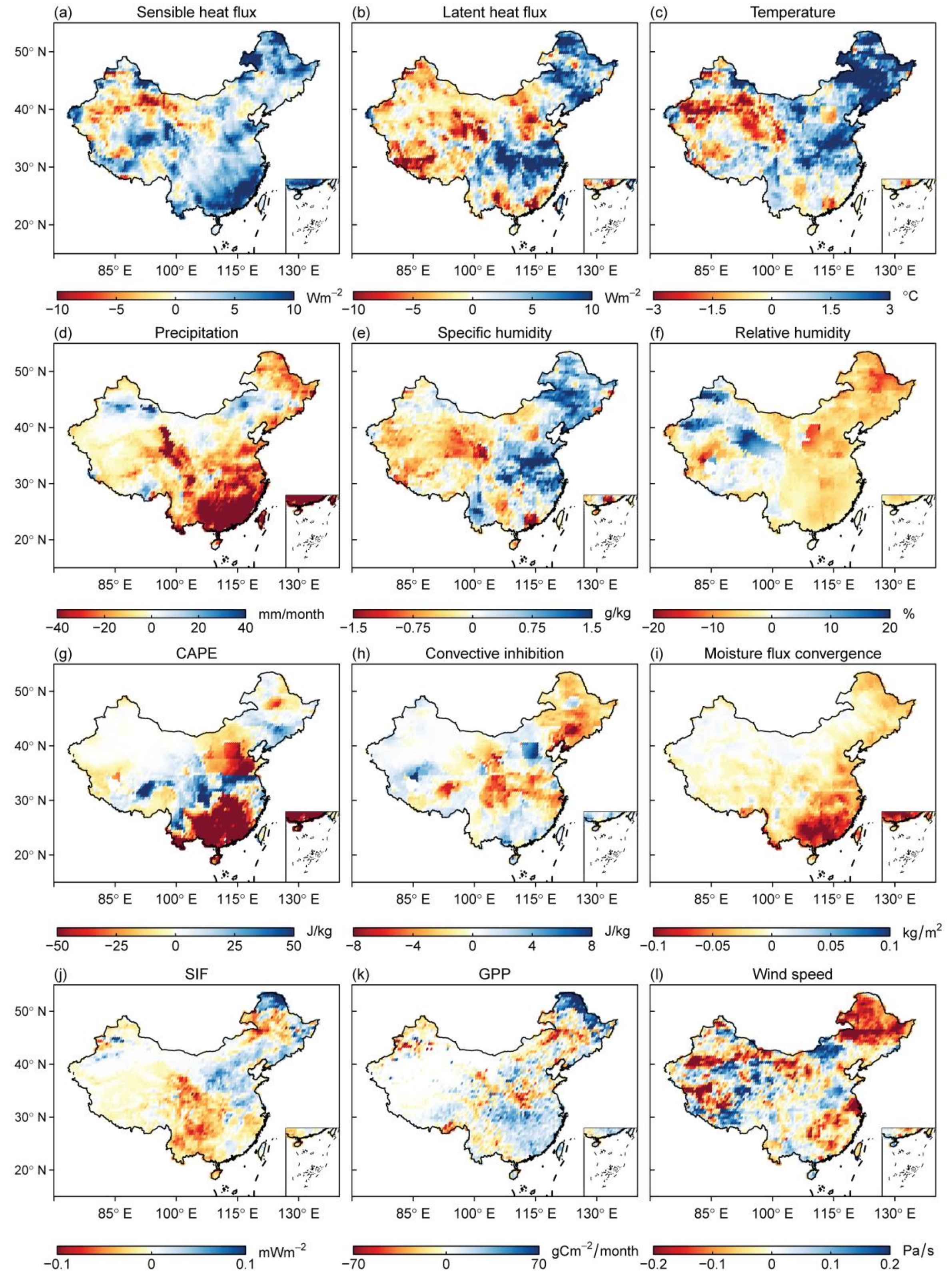

Fig. 2. Average differences of monthly meteorological factors and ecosystem productivity between dry/wet conditions in China. Results from ERA5 reanalysis dataset (a), (b), (e), (h), (i), (l); results from 20 CR dataset (c), (d), (f), (g); results from SIF and GPP (j)-(k). The differences are calculated by subtracting the mean values of variables obtained under drought conditions from those obtained under wet conditions.

We then investigate the effects of drought events on the ecosystem carbon budget by calculating the anomalies of SIF and GPP (Fig. 2j, k). The anomalies of SIF and GPP are both negative in most regions (i.e., northwestern, southwestern, and northeastern central areas) under drought conditions, except in parts of northeastern and central China (Deng et al., 2021; Li et al., 2019). In southeastern China, however, the GPP shows positive results unlike SIF. Although GPP based on the vegetation photosynthesis model (VPM) provides a reliable GPP estimation for non-forest natural vegetation and cropland (Yuan et al., 2015), its estimation in ENF and EBF (mainly in southeastern China) is accompanied with high uncertainty compared with other GPP products (Mercado et al., 2009; Dong, 2017), which may be related to the higher light use efficiency for diffused radiation. Overall, the results of SIF are similar to GPP in western and northern China but show differences in other regions. The potential for dryness-related carbon loss, therefore, needs to be understood when exploring the impacts of concurrent extreme climatic events on ecosystems (Nemani et al., 2003; Zhou et al., 2019a). In addition, similar results are found for changes in GPP and the machine-learning-generated SIF, emphasizing the robustness of our main results.

3.2 Sensitivity analysis of TWSA-DSI to meteorological variables under climate change

Fig. 3 shows the percent variation of TWSA-DSI to meteorological variables during 2002-2021, which demonstrates considerable spatial variability. We remove non-vegetated regions (e.g. desert regions) based on Vegetation zoning data for China from Resource and Environment Science and Data Center (https://www.resdc.cn) in China. As Fig.3 shows, RH (with 1 SD perturbed) has a significant positive impact on TWSA-DSI over 90% of areas, with the highest sensitivity up to 64.6%, especially in coastal areas (Fig. 3e), while the sensitivity of T_{2m} with 1 SD perturbed ranges from -47.5% to 22.7% (Fig. 3h). In most areas, the sensitivity of the TWSA-DSI to some variables is positive, including precipitation, snowfall, rsds, T_{dew} and wind speed (Fig. 3a, b, g, i, j), such as the mean absolute value of the sensitivity of precipitation to TWSA-DSI is 30.9%. In contrast, specific humidity, ps, T_{2m} and rlds are negatively correlated with TWSA-DSI in most parts of China, except for the Qinghai-Tibet Plateau and South China (Fig. 3d, c, h, f).

To explore possible shifts in the sensitivity patterns, we evaluate the driving effect of each factor on drought events under CMIP6 during the historical and future periods (Fig. S2-S4). Precipitation, RH and T_{2m} are the main controlling factors for future drought development in most areas under SSP126, with the range of sensitivity for each factor with 1 SD perturbed from 0.25% to 59.2%, from -2.03% to 47.7% and from -20% to 6.3%, respectively (Fig. 4). Specific humidity is shown to switch from a negative to a positive correlation with TWSA-DSI across most of China in the future due to the warming climate (Fig. 3e, Fig. 4e). Additionally, air temperature and T_{dew} also show a similar transition from positive to negative sensitivity in southeastern China. Meanwhile, wind speed, rlds and rsds show a negative sensitivity trend in most areas. Overall, the future distribution pattern of sensitivity of climate variables is generally towards negative sensitivity compared to GRACE/GRACE-FO, except for precipitation, RH and specific humidity. Especially, the effects of precipitation, relative humidity and temperature are even more significant in the future and precipitation becomes the most influential factor driving TWSA-DSI, but drought is influenced by a combination of factors and can only be assessed robustly by considering the different mechanisms at play.

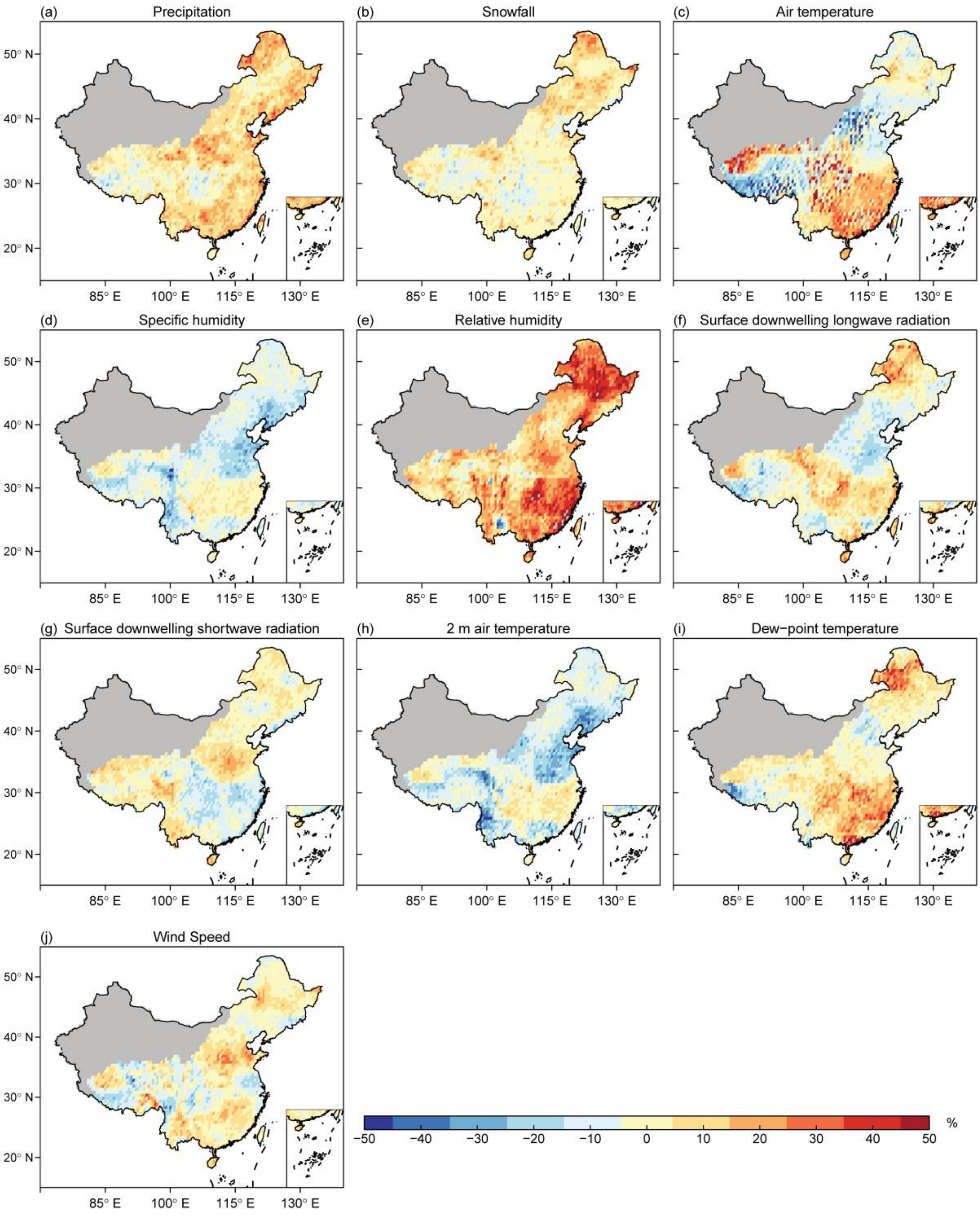

Fig. 3. RF sensitivity analysis results. Sensitivities represent the percent change in TWSA-DSI due to a perturbation of each variable by +1 SD (data source: ERA5 reanalysis dataset). Grey denotes desert regions.

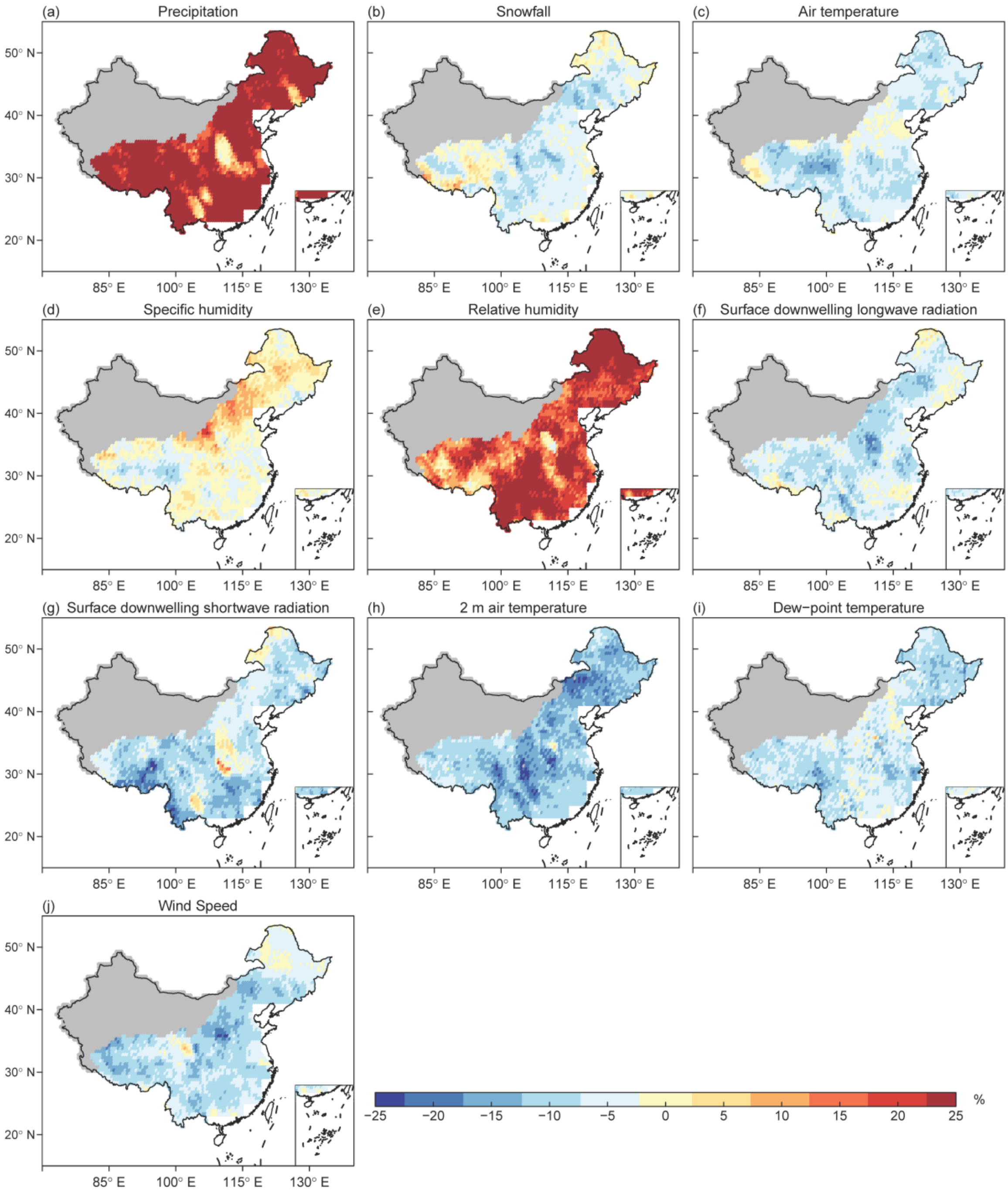

Fig. 4. RF sensitivity analysis results. Sensitivities represent the percent change in TWSA-DSI due to a perturbation of each variable by +1 SD (data source: CMIP6 under SSP126). Grey denotes desert regions.

3.3 Water stress impacts on ecosystem carbon uptake

To explore the effects of droughts on the carbon sink, we investigate the impacts of heat and water stress on ecosystem carbon uptake using FLUXNET 2015 dataset and China FLUX dataset. We first calculate the Pearson's correlation coefficient between carbon flux (i.e., GPP, TER, and NEP) and environmental variables (T_{air}, SM and TWSA) in the warm season (i.e., when the 7-day mean temperatures exceed the 60th percentile of the daily temperature at each site) (Fig. 5a-d). Then, after detrending anomalies of climate variables and fluxes, we evaluate the sensitivity of carbon flux to environmental variables with warming T_{air} (Fig. 5e-s). In the warm season, NEP is negatively correlated with T_{air} in CRO and GRA, positively in EBF and MF, while TER only shows a negative correlation with T_{air} in MF and GPP is not significantly correlated with T_{air} in CRO and MF (Fig.5a-d). The detrended anomaly analysis indicates that the sensitivity of TER to T_{air} increases with increasing temperature in all land cover types (i.e., there is a positive correlation between TER sensitivities to temperature anomalies throughout the study period). In contrast, the sensitivities of GPP and NEP to T_{air} decrease with increasing temperature in EBF, CRO and GRA (Fig. 5e, g, n, p, q, s), except for MF (Fig. 5k, m). These results imply that the TER is less sensitive to heat stress than GPP and NEP under warmer conditions, highlighting the crucial role of heat stress in constraining carbon assimilation. More importantly, the ecosystem complexity also has a significant effect on carbon sink capacity. The forest ecosystems (i.e. EBF and MF) not only have a stronger ability to increase carbon allocation to root growth than stem and leaf growth, but can also regulate stomatal conductance and maintain productivity, which can mitigate excessive water loss (Wolf et al., 2013). In contrast, the grass ecosystem (i.e. GRA and CRO) has lower productivity than forests with a simpler structure, thus the aboveground parts are more likely to wither under heat stress (Stampfli et al., 2018). Furthermore, as drought also influences the carbon budget by limiting plant growth rate through water stress (Jha and Srivastava, 2018), we also evaluate the responses of carbon fluxes (i.e., the sensitivity of GPP, TER, and NEP) to the anomalies of TWSA and SM in the different ecosystems (Fig. S5-S6).

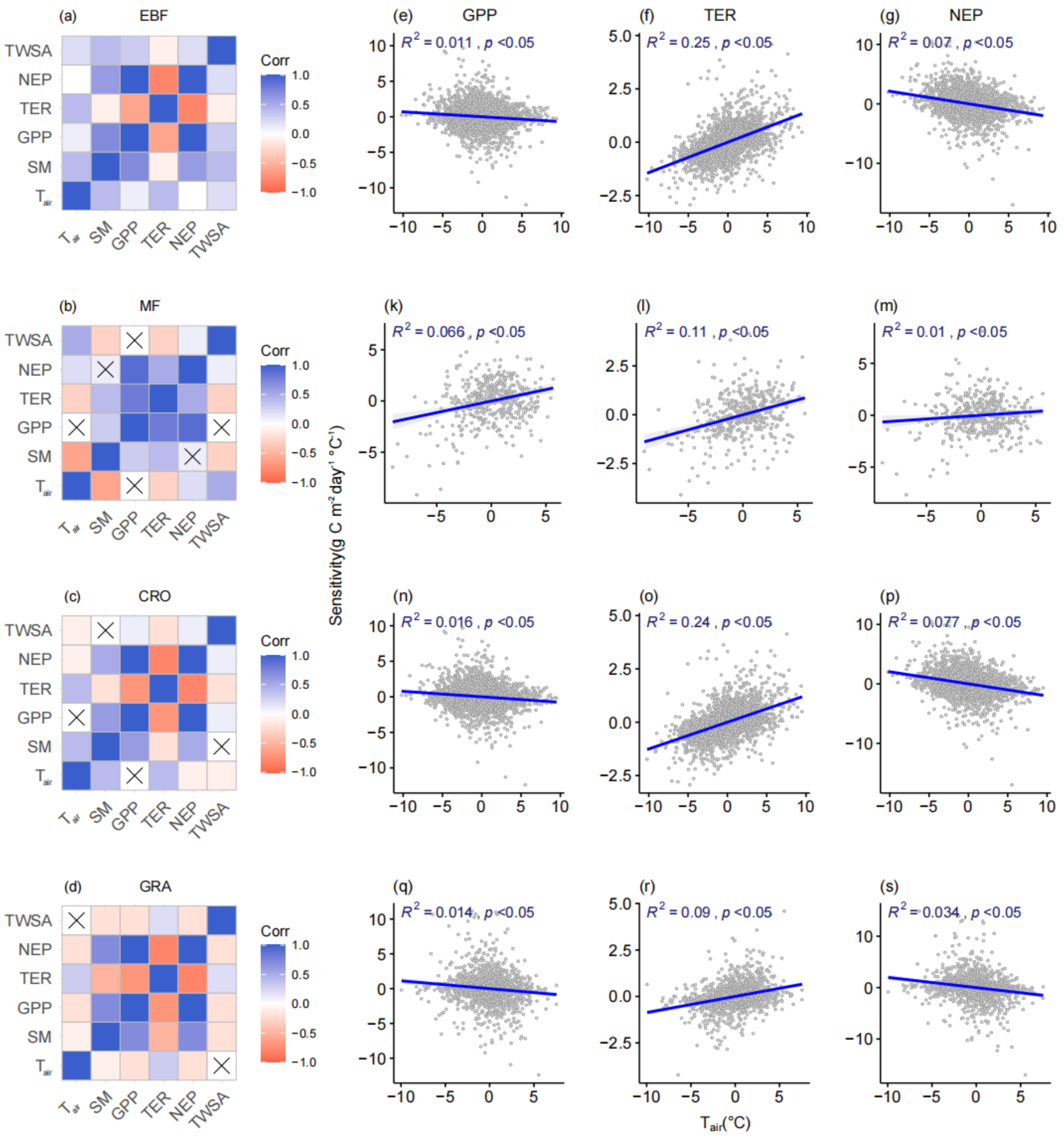

Fig. 5. Pearson's correlation coefficient of carbon flux (i.e., GPP, TER, and NEP) and environmental variables (T_{air}, SM and TWSA) in the warm season. The symbol X means that the correlation is not significant at 0.05 level (a-d). The sensitivities of carbon flux anomalies to T_{air} anomalies (g C m^{-2} day^{-1} °C^{-1}; shown on the y-axis) and the mean daily temperature anomaly (°C; x-axis) in different ecosystems (rows: evergreen broadleaf forest (EBF), mixed forest (MF), grasslands (GRA), and croplands (CRO)) (e-s).

As before, the association between the sensitivities of carbon fluxes to SM or TWSA anomalies differ across the four land cover types, but the results for TWSA and SM are largely consistent. The carbon fluxes to TWSA anomalies increase with higher TWSA in all ecosystems. Likewise, the results for SM are the same as TWSA in GRA and CRO, whereas GPP, TER and NEP are negatively correlated with SM in EBF and MF (Fig S5). The results reveal that the carbon fluxes in the grass ecosystems (i.e., GRA and CRO) are highly affected by water stress because grass ecosystems have a weaker ability to increase carbon allocation to the root growth than forests, so the ecosystem cannot hold enough water to supply plants' photosynthesis (Fig. S5-S6). Therefore, the GRA and CRO ecosystems are more sensitive to water stress than EBF and MF, indicating that the forest structure is more complicated and the carbon sink function is stronger.

3.4 Observed and projected changes in drought conditions and their effects on carbon uptake

The GRACE/GRACE-FO dataset (2002-2021) shows similar spatial and temporal characteristics of drought, with a strong increase in drought events in southeast and northwest China. Moreover, it is noteworthy that the North China Plain and certain northwestern regions experience the least frequent droughts, which are also the longest and most severe (Fig. 6a-i). For example, the North China Plain is one of the areas that are extremely dependent on groundwater resources (Gong et al., 2018). However, due to groundwater over-exploitation for many years, climate change and human activities, droughts are increasing in frequency, duration and severity (Wang et al., 2020b). Further, the land cover of these areas is primarily grassland or cropland (Fig. 1) which have weaker drought resistance and a longer post-drought recovery time than forests and shrubs (Li et al., 2019). Therefore, these regions are less resilient (i.e., a significant deviation from the norm) to drought than other areas, leading to more intense and long-lasting drought. Drought indicators (i.e., frequency, duration, severity) have increased in northern, north-western and south-western China over the century (Fig. 6j-6l), but decreased in other regions. In Southwest China, the Qinghai-Tibet Plateau, and Northwest and Northern China, drought duration has doubled, and the severity of droughts has increased by more than 80%.

The TWS simulations obtained under the CMIP6 framework are then used to project future drought characteristics and evolution. Projections of drought frequency show significant spatial heterogeneity; most areas in Southwest China and Northeast China are expected to continue drying, while Northwest China and East China exhibit a significant wetting tendency (Fig. 7). Drought occurrence is projected to increase fourfold over half of China in the late 21st century, and drought frequency is projected to increase sixfold over 62.51% of the country under all SSPs by the middle of the 21st century (Fig. 7 a-b, d-e, g-h).

China is projected to experience an increasing intensification of drought conditions as the climate warms with increasing carbon emissions. For example, under SSP585 over 58.74% of areas exhibit positive drought frequency trends, compared to 52.31% and 20.92% under SSP370 and SSP126. Similarly, the areas with an increasing trend in drought frequency and intensity under the SSP585 are both approximately 8% and 35% higher than under SSP126 and SSP585 respectively (Fig. 7c, f, i and Fig. S7-S9). Moreover, under the lowest emissions path, the North China Plain shows a significant wetting trend, while this region tends to be drier under a high emission scenario. This suggests that with increasing carbon emissions the uneven distribution of water resources is likely to be further intensified, and extreme drought or flooding hazards might occur more frequently.

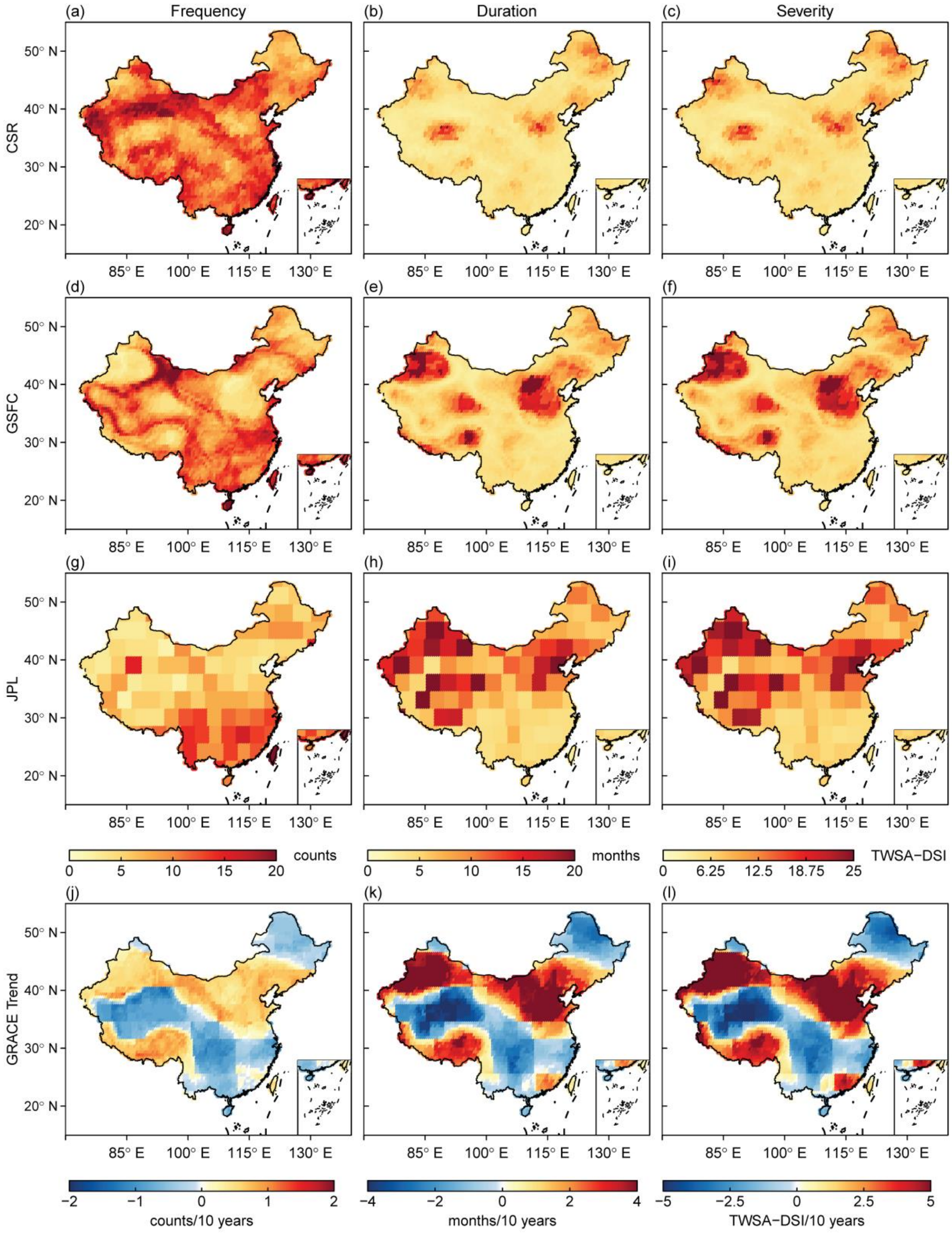

Fig. 6. Statistics of TWSA-based drought indicators from 2002-2021 (i.e., drought frequency, drought duration, drought severity) obtained from CSR, GSFC, and JPL satellites, respectively (a)-(c), (d)-(f), (g)-(i) and their trends based on the mean of TWSA from three GRACE satellites in China during 2002-2021 (j)-(l).

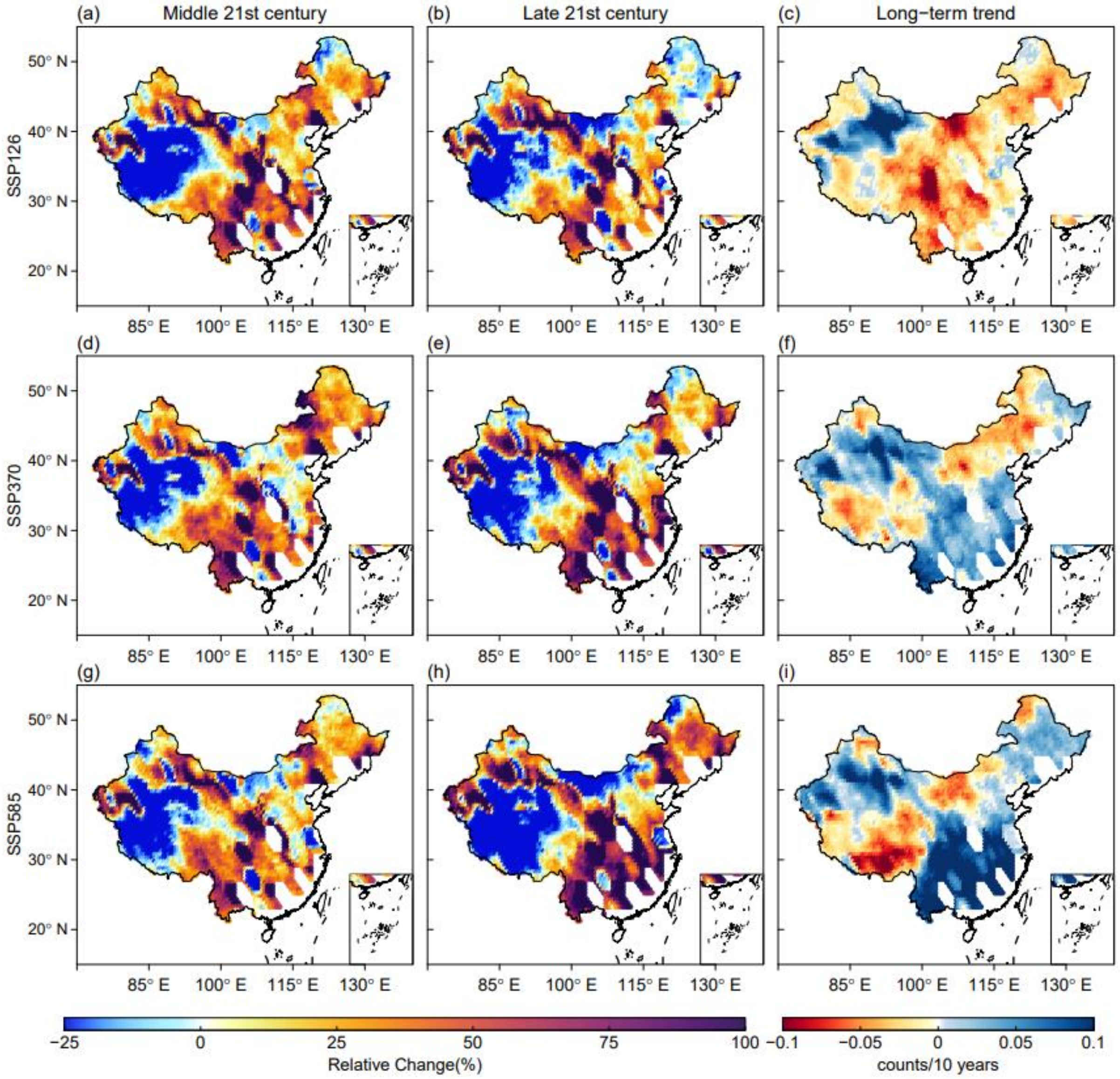

Fig. 7. Future changes and trends in the characteristics of drought frequency under three different SSPs in China. Relative changes from the historical period to the middle 21st century (2031–2060) (a), (d), (g); Relative changes from the historical period to the late 21st century (2071-2100) (b), (e), (h); and long-term trend in the number of droughts per decade during 2015–2100 (c), (f), (i).

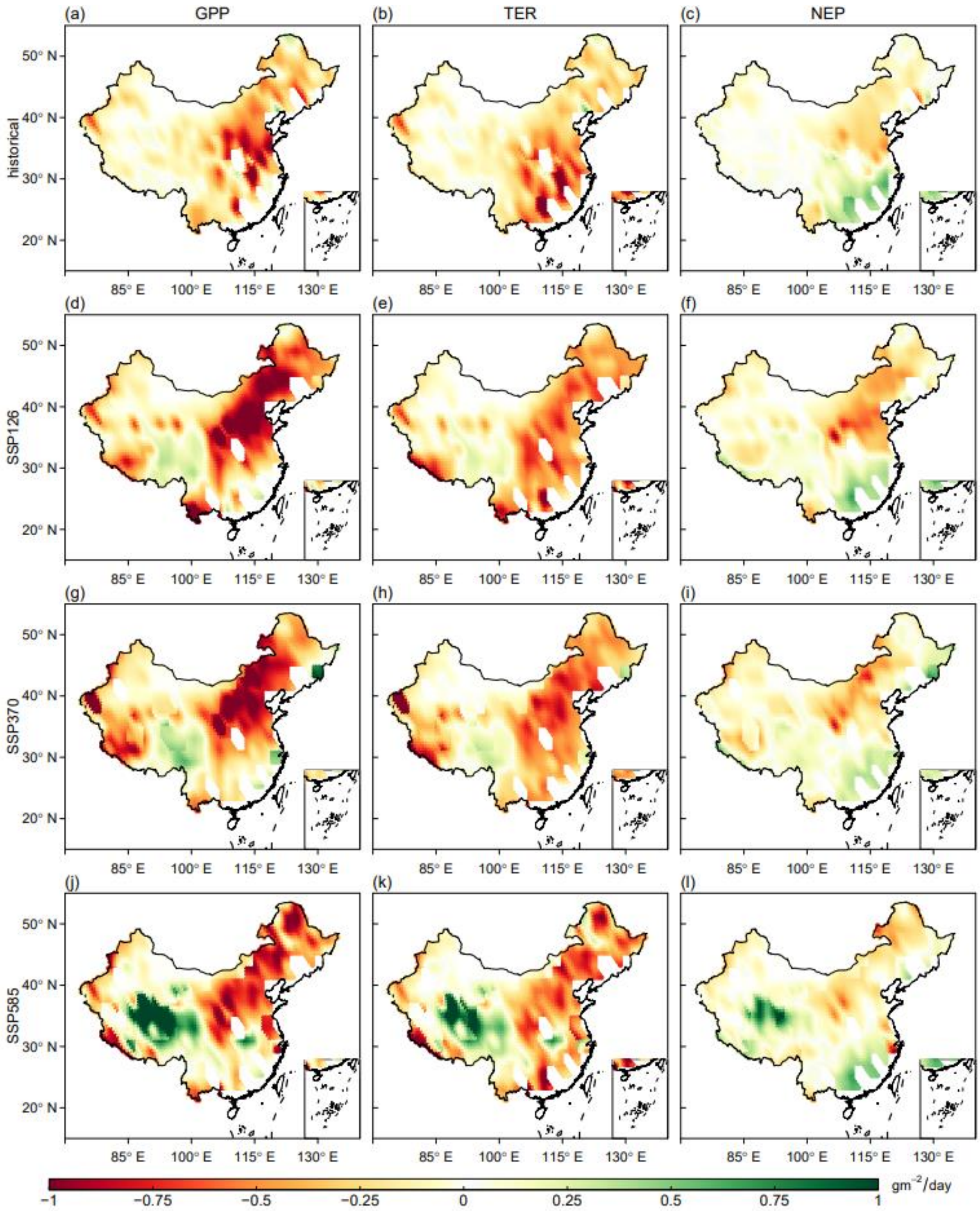

Fig. 8. Historical and future anomalies of GPP, TER, and NEP during drought events. Anomalies in the historical period (1985-2014) (a)-(c); anomalies in the future period (2071-2100) under the three SSPs (d)-(l).

To further project the impact of future droughts on the ecosystem carbon budget, we use TWS simulated by the H08 model forced by outputs from five CMIP6 GCMs (i.e., M6A-LR, GFDL-ESM4, MPI-ESM1-2-HR, MRI-ESM2-0 and UKESM1-0-LL) under three SSPs to analyze the anomalies of the historical (1985-2014) and future (2071-2100) carbon budget (i.e., deviation of a variable from its base period average) under drought conditions in the growing season. Under future warming conditions, we find GPP, TER and NEP tend to be significantly constrained by drought (Fig. 8). Although the TER show negative anomalies in most areas under drought stress, the significant reduction in GPP results in NEP still shows a negative anomaly overall. The average percentage of negative anomalies of GPP (NEP) across China under the three SSPs is 76.63% (61.95%), compared with 89.80% (64.13%) during the historical period. Although the proportion of negative anomalies in GPP (NEP) is higher in the historical period than in the future period, the negative anomalies are lower in the future period than that in the historical period. The mean negative anomaly of GPP (NEP) under the three SSPs was -0.42 (-0.16) $g \cdot m^{-2} \cdot day^{-1}$, compared to -0.23 (-0.09) $g \cdot m^{-2} \cdot day^{-1}$ for the historical period. Moreover, the overall NEP across China is reduced by about two-fold under SSP126 as much as under SSP585. It is worth noting the positive anomalies of carbon uptake in the Tibetan Plateau.

As shown in Fig 7, future droughts based on TWSA-DSI are projected to mitigate in the Tibetan Plateau. Under higher carbon emission scenarios, the decreasing rate of drought is more significant. These results suggest a wetting tendency regarding higher TWS in the Tibetan Plateau due to melting glaciers and permafrost and increased precipitation under global warming, which is consistent with previous projections (Pokhrel et al., 2021; Chen et al., 2022). The TWS derived from the H08 model simulates the key terrestrial hydrological (for example, soil, and vegetation) processes, which is the direct water pool of plants and determines the amount of water extracted by plant roots, so it can provide a versatile tool to represent future water condition for plant growth (Pokhrel et al., 2021; Padiyedath Gopalan et al., 2022). Moreover, we also evaluate the responses of carbon fluxes (i.e., the sensitivity of GPP, TER, and NEP) to the anomalies of TWSA and SM in the different ecosystems (Fig.S5-S6) and find that the results are largely consistent. Water stress has a significant impact on ecosystem productivity, which may induce plants to close stomata to minimize water loss at the leaf scale and can further constrain plant photosynthesis in ecosystems (Liu et al., 2020; Li et al., 2021). Although the Tibetan Plateau is a fragile grassland ecosystem with lower productivity than forest and coastal wetlands and is very sensitive to water stress under climate change (Xiao et al., 2013; Zhang et al., 2023), future reductions in drought might mitigate the effects of water stress on GPP and thus enhancing photosynthesis. Sun et al. (2019) also highlighted that future warming will enhance the GPP and TER of the ecosystem in the Tibetan Plateau. In addition, rising temperatures, precipitation and nitrogen availability might further drive GPP increases, leading to increased carbon uptake on the Tibetan Plateau (Zhao et al., 2018). However, the relationship between TWS and GPP on Tibetan Plateau is extremely complex. For example, the remote sensing data shows that grasslands on the Tibetan Plateau is very sensitive to droughts with low soil moisture, especially when it is compounded with high temperature (Zhang et al., 2023). It is highly uncertain that whether permafrost degradation would result in wetting or drying of surface soil, nor these changes would facilitate vegetation growth or lead to grassland degradation. We also know little about how the melting glacier and the associated hydrological changes would affect vegetation growth, especially the grasslands. Therefore, future work can be devoted to exploring how glacial melt and associated hydrological changes would affect vegetation growth in the Tibetan Plateau.

Recently, GCMs have been widely used to quantify climate change impacts on hydrological fluxes and storages, especially the projections of water storages from TWS components (i.e., soil moisture and snow) (Pokhrel et al., 2014, 2021; Jensen et al., 2019). Considering the differences among different GCMs, Fig S10 shows the future mean anomalies of GPP during droughts under the three SSPs from five CMIP6 GCMs, and we find that the 5 GCMs also have similar positive anomalies of carbon uptake in the Tibetan Plateau, which is consistent with Fig 7. Although GCMs show substantial uncertainties in the Tibetan Plateau, the overall distribution of GPP anomalies in each GCM is basically consistent. Therefore, we use the averaged results of the five GCM models to improve the robustness of our main conclusions. Overall, the Tibetan Plateau is predicted to continue functioning as a net carbon sink, despite ongoing severe permafrost degradation under global warming, which is consistent with previous studies (Pokhrel et al., 2021; Chen et al., 2022). Drought stress is likely to significantly damage the carbon sink in China, and the effect of drought is projected to increase as greenhouse gas emissions increase. Therefore, drought is one of the major causes of future changes in the terrestrial carbon sink.

4. Discussion

4.1 Evaluating the performance of machine learning on TWS simulations

To investigate the main factors controlling drought events, we perform a sensitivity analysis by interpreting the contribution of each meteorological variable to the TWSA-DSI using both observational data and simulations during historical and future periods. To evaluate the robustness of our RF models, we selected five indices, including Pearson correlation coefficient (PCC), Nash-Sutcliffe Efficiency (NSE), Normalized root Mean square error (NRMSE), Mean square error (MSE) and Mean Absolute Percentage Error (MAPE) (Text S1). Fig. 9a shows the mean TWSA-DSI time series over China reconstructed by our machine learning model during 2002-2021, which are compared with the GRACE/GRACE-FO observations (the mean TWSA series from CSR, GSFC, and JPL satellites). The results show that our RF model performs well over the study period with high PCC (0.99) and NSE (0.87). The simulations show a high spatial agreement with GRACE observations, where the mean MSE is 0.2 mm^2 and the mean MAPE is less than 0.15% (Fig. 9b-e).

We evaluate the performance of TWS simulations in eight different geophysical regions and we find that seven of the regions show a high correlation (PCC>0.6) between our RF-based TWSA-DSI reconstruction and the GRACE/GRACE-FO observations (Fig. 9f-m).

Additionally, we also evaluate the accuracy of our TWSA-DSI machine learning reconstructions driven by the CMIP6 historical and future simulations (Fig. S11-S12). The results also suggest a high consistency of our RF-based reconstruction with CMIP6 datasets during the historical and future periods.

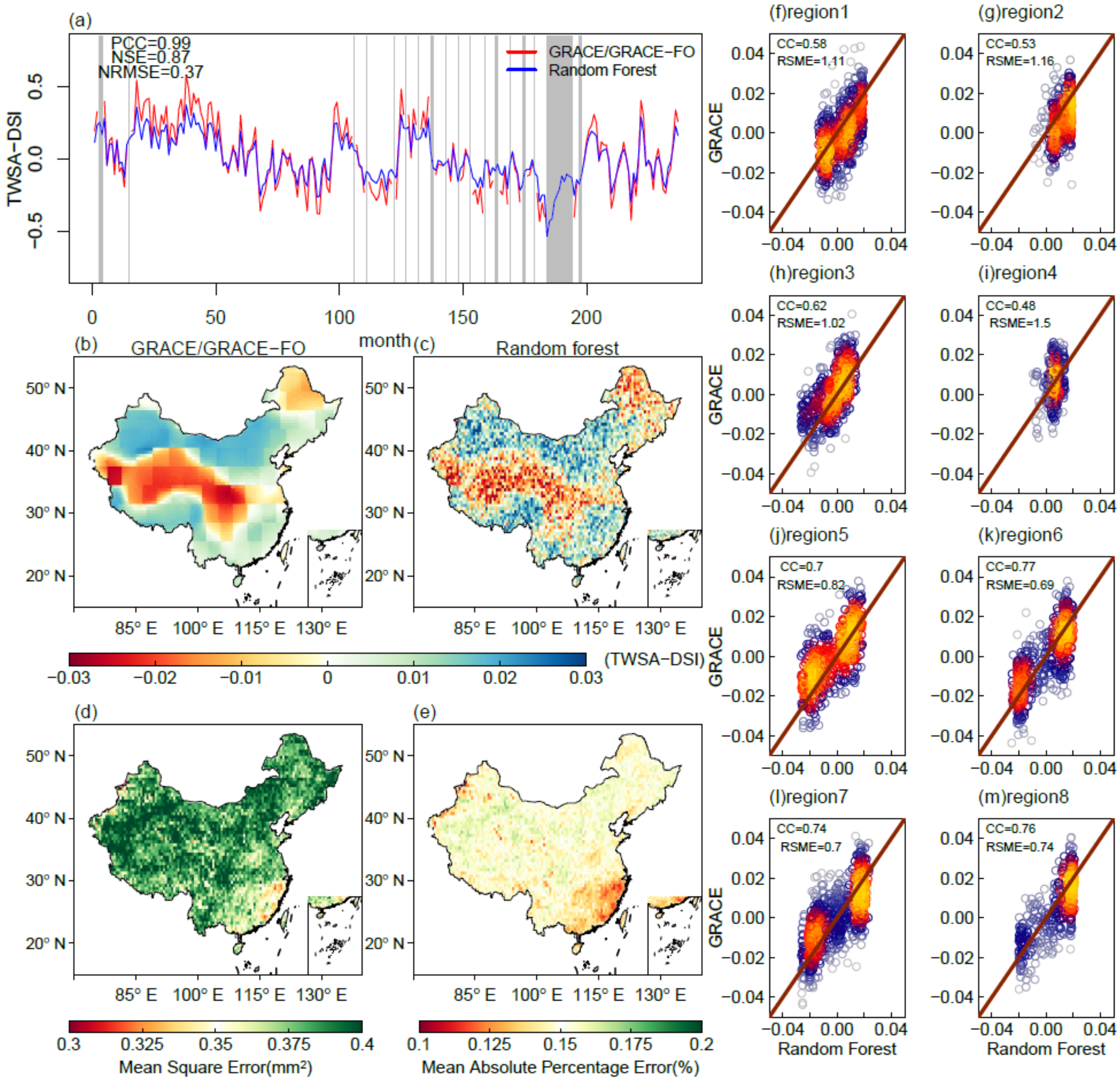

Fig. 9. Evaluation of the accuracy of random forest-based TWSA reconstructions. Evaluation of the mean TWSA-DSI time series during the period 2002-2021 using PCC, NSE and NRMSE. (a); comparison of reconstructions with GRACE observations (b)-(c); spatial evaluation using MSE and MAPE (d)-(e); evaluation of the accuracy in eight regions using PCC and RMSE (f)-(m).

4.2 Comparisons of CMIP6 and CMIP5 projections

Drought is one of the most harmful threats to forest carbon sinks, and can cause significant declines in GPP in forest ecosystems at regional and continental scales (El-Madany et al., 2020;

Xu et al., 2020). To further investigate the relationship between drought and ecosystem carbon sink, we also analyze future anomalies in GPP, TER and NEP under drought conditions during the growing season under three RCPs (e.g., RCP2.6, RCP6.0, RCP8.5) from the CMIP5 framework (Fig. S13). Negative GPP (NEP) anomalies are found over 54.1% (51.4%) of China under RCP8.5; the negative GPP anomalies are found 60.2% of China on average under the three RCPs, while the NEP is 56.72%. In addition, under RCP8.5, the overall negative NEP in China is about twice as strong as under RCP2.6 and 1.5 times under RCP6.0 (Fig. S13). Moreover, we calculate the relative changes in GPP, TER and NEP in the future without considering the effects of droughts. As shown in Fig. S14, the carbon flux of the future ecosystem is projected to increase significantly in most areas compared to the historical period. Under drought stress, however, the results are exactly the opposite (Fig. 8). Therefore, we find drought is an important factor in limiting the terrestrial carbon sink. The results indicate that the function of the carbon sink in China is likely to strengthen during the growing season without the effect of drought events. However, the increase in GPP (NEP) is significantly reduced under drought stress, and the degree of decline is projected to increase as the concentration of carbon emissions increases, which further demonstrates that drought is an important factor in limiting the terrestrial carbon sink. In locations with grassland, farmland and other vegetation with shallow roots, the soil cannot hold enough water to sustain photosynthesis and evapotranspiration during the dry season, which may lead to soil water stress, stomatal closure and further reduction in photosynthesis (Ichii et al., 2007; de Graaff et al., 2014).

Meanwhile, the anomalies of GPP, TER and NEP are also projected using the CLM4.5 land surface model forced by bias-corrected GFDL-ESM2M climate data, and these individual assessments confirm that the limited water availability is likely to constrain the future carbon sink (Fig. S15). Under drought conditions, photosynthesis and respiration are both reduced, as detected by strong negative anomalies of GPP, TER and NEP in most of China, implying large reductions in ecosystem carbon uptake in a future warmer climate. Overall, the CMIP5 results (Fig. S13-15) are generally consistent with CMIP6 simulations, supporting the robustness of our main results. The projected reductions in carbon uptake during drought events occur alongside an overall increase in carbon sink due to CO_2 fertilization (Campbell et al., 2017; Wang et al., 2020b). This paradox can be explained by the fact that in some regions (e.g., southeastern China in Fig. 8c, f), the effect of CO2 fertilization on GPP is offset by various factors (e.g., human activity, different landforms and changes in climate conditions), further leading to a decrease in GPP (Yin et al., 2023c). However, despite the decrease in GPP under drought stress in these areas, the significant decrease in TER (i.e., reduced CO2 emission capacity) is the cause of the increase in NEP. Overall, the negative anomalies of NEP in most areas are similar to GPP under drought stress (Fig. 8). Our results indicate that ecosystem carbon sink processes are influenced by multiple factors; GPP and NEP are more sensitive to heat and drought stress than TER, but ecosystem complexity also has a significant effect on carbon sink capacity. Therefore, it is only by considering the mechanisms of multiple factors simultaneously that the interactions between ecosystem carbon budget and terrestrial-atmospheric conditions can be disentangled.

4.3 Uncertainty and limitations

Climate projections are essential for decision-making but contain non-negligible uncertainty (Chai et al., 2022). To investigate the uncertainty sourced from different procedures, we use the multivariate ANOVA method to decompose the uncertainty contribution of different sources (Addor et al., 2014; Wang et al., 2020a). Fig. 10 shows the sources of uncertainty under CMIP6-based projections, including three SSPs, GCMs and their interactions, contributing to the overall uncertainty of projected drought frequency, duration and severity. Moreover, the multiple sources of uncertainty for eight different geophysical regions are calculated respectively.

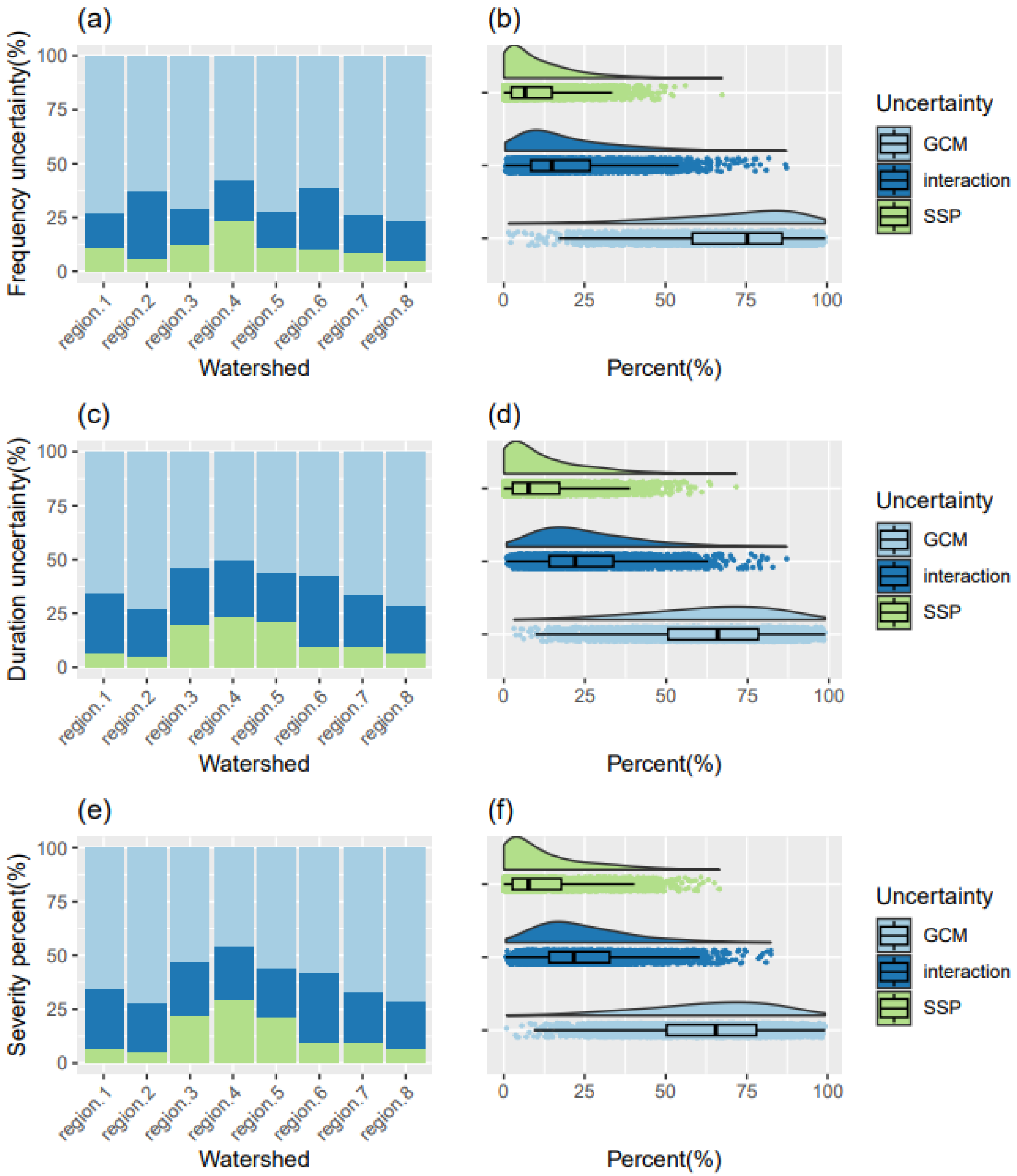

Fig. 10. Uncertainty analysis of drought frequency, duration and severity in China based on three SSPs, GCMs and their interaction. The uncertainty distribution of the two sources and their interaction in 8 regions (a, c, e); the uncertainty percentage distribution of the two sources and their interaction in mainland China (b, d, f).

The influence of GCM uncertainty accounts for the largest proportion of uncertainty, and is larger than that of the SSPs and their interaction (Fig. 10). We also analyze the sources of uncertainty in GPP, TER, and NEP from the CMIP5 and CMIP6 datasets, and again find the total variance of drought indicators and carbon budget variables mainly arises from internal variability and model uncertainty (Fig S16-S17). The relative contribution of interaction variation uncertainty decreases with the increased contribution of model uncertainty (GCM), and the scenario uncertainty (SSP and RCP) increases slowly. Our results indicate that climate uncertainty (i.e., GCMs and emission scenarios) is the major source of uncertainty in projecting future drought events, and so improving the accuracy of model projections remains the best way to reduce uncertainty in climate change impact studies.

Some limitations should be emphasized. Although we tried to include as many relevant features as possible to train our random forest model and achieve high simulation accuracy, the complex relationships between these variables and the uncertainty in the model caused by human and geophysical factors need to be further explored. As drought generation mechanisms are also influenced by other factors, future research should aim to reveal the coupling between them. In addition, the limited number of observation sites in the FLUXNET dataset may affect the accuracy of the results and the use of a larger number of GCMs might increase the robustness of global and component uncertainty, so the mobilization of computational resources to calibrate as many observation sites as possible and constrain the uncertainty of GCMs for future work is also the next priority.

5. Conclusions

In this study, we attribute and explain the physical mechanisms of TWSA-based drought conditions and ecosystem carbon exchanges in response to drought stress in China. Heat and water stress have a significant effect on carbon uptake. We find that GPP and NEP are more sensitive to heat and water stress than TER, and the ecosystem complexity also has a significant effect on carbon sink capacity. In addition, drought conditions are projected to become more severe over half of China under the three future SSPs, with the frequency, duration and severity of extreme drought events significantly increasing by more than sixfold in more than 60% of Chinese regions.

Under future stronger drought events, NEP is projected to show negative anomalies over most of China in the future. Under drought stress, the negative GPP (NEP) anomalies cover 76.63% (61.95%) of China on average under the three SSPs, which means that the regulation of ecosystem carbon sinks by droughts is projected to weaken over 60% of China. Mean minimum negative anomalies of GPP (NEP) are projected at -0.42 (-0.16) $g \cdot m^{-2} \cdot day^{-1}$ under the three SSPs compared to -0.23 (-0.09) $g \cdot m^{-2} \cdot day^{-1}$ for the historical period, suggesting that the negative effect of drought on the carbon sink is likely to strengthen as greenhouse gas emissions increase.

Precipitation, relative humidity and temperature are the primary drivers of droughts in most of China based on the random forest method. The variance of the drought indicators and carbon budget variables arises mainly from the uncertainty of the climate models and emission scenarios. As the contribution of the climate models to the overall uncertainty increases, the relative contribution of the interaction variation between models and scenarios decreases, while the scenario uncertainty increases slowly. Overall, higher carbon emissions are projected to lead to stronger drought impacts on vegetation carbon assimilation, and the decrease of GPP caused by drought is the main reason for the change in the terrestrial carbon sink.

Under future warming climates, the regulation function of the ecosystem carbon sink is likely to be weakened by droughts. Higher carbon emissions scenarios tend to be accompanied by increasingly detrimental impacts on the terrestrial carbon sink. This work highlights the need to focus on better understanding the risks posed by droughts for the sustainable development of ecosystems. As an increase in the likelihood of future droughts seems inevitable, there is an urgent need to improve ecosystem resilience to future warming climates.

Author contribution

Y.Y. and J. Y. conceived and designed the study. Y.Y. processed the model simulations

and reanalysis data. Y.Y., S.K., Y.Y., L.S., X.G., and A.V. contributed to the data analysis and interpretation. Y.Y. drafted the manuscript. All authors reviewed and edited the manuscript.

Declaration of Competing Interest

The authors declare no competing interest.

Acknowledgements

J.Y. acknowledges support from the National Natural Science Foundation of China (Grant NOs. 52009091; 52242904) and the Fundamental Research Funds for the Central Universities (NO. 2042022kf1221). LJS is supported by UKRI (MR/V022008/1) and NERC (NE/S015728/1). The numerical calculations in this paper have been performed on the supercomputing system in the Supercomputing Center of Wuhan University.

Reference

Addor, N., O. Rössler, N. Köplin, et al. 2014. Robust changes and sources of uncertainty in the projected hydrological regimes of Swiss catchments. Water Resour. Res. 50:7541–7562. doi:10.1002/2014WR015549.

Breiman, L. 2001. Random Forests. Mach. Learn. 45:5–32. doi:10.1023/A:1010933404324.

Brodribb, T.J., J. Powers, H. Cochard, et al. 2020. Hanging by a thread? Forests and drought. Science 368:261–266. doi:10.1126/science.aat7631.

Campbell, J.E., J.A. Berry, U. Seibt, et al. 2017. Large historical growth in global terrestrial gross primary production. Nature 544:84–87. doi:10.1038/nature22030.

Chai, Y., Y. Yue, L.J. Slater, et al. 2022. Constrained CMIP6 projections indicate less warming and a slower increase in water availability across Asia. Nat. Commun. 13:4124. doi:10.1038/s41467-022-31782-7.

Chang, X., Y. Xing, W. Gong, et al. 2023. Evaluating gross primary productivity over 9 ChinaFlux sites based on random forest regression models, remote sensing, and eddy covariance data. Sci. Total Environ. 875:162601. doi:10.1016/j.scitotenv.2023.162601.

Chen, H., P. Ju, Q. Zhu, et al. 2022. Carbon and nitrogen cycling on the Qinghai–Tibetan Plateau. Nat. Rev. Earth Environ. 3:701–716. doi:10.1038/s43017-022-00344-2.

Chen, X., L. Wang, Z. Niu, et al. 2020. The effects of projected climate change and extreme climate on maize and rice in the Yangtze River Basin, China. Agric. For. Meteorol. 282–283:107867. doi:10.1016/j.agrformet.2019.107867.

Chu, H., D.D. Baldocchi, R. John, et al. 2017. Fluxes all of the time? A primer on the temporal representativeness of FLUXNET. J. Geophys. Res. Biogeosciences 122:289–307. doi:10.1002/2016JG003576.

Compo, G.P., J.S. Whitaker, P.D. Sardeshmukh, et al. 2011. The Twentieth Century Reanalysis Project. Q.

J. R. Meteorol. Soc. 137:1–28. doi:10.1002/qj.776.

Dannenberg, M.P., D. Yan, M.L. Barnes, et al. 2022. Exceptional heat and atmospheric dryness amplified losses of primary production during the 2020 U.S. Southwest hot drought. Glob. Change Biol. 28:4794–4806. doi:10.1111/gcb.16214.

Deng, Y., X. Wang, T. Lu, et al. 2023. Divergent seasonal responses of carbon fluxes to extreme droughts over China. Agric. For. Meteorol. 328:109253. doi:10.1016/j.agrformet.2022.109253.

Deng, Y., X. Wang, K. Wang, et al. 2021. Responses of vegetation greenness and carbon cycle to extreme droughts in China. Agric. For. Meteorol. 298–299:108307. doi:10.1016/j.agrformet.2020.108307.

Dong, J. 2017. A global moderate resolution dataset of gross primary production of vegetation for 2000-2016. doi:10.6084/m9.figshare.c.3789814.v1.

El-Madany, T.S., A. Carrara, M.P. Martín, et al. 2020. Drought and heatwave impacts on semi-arid ecosystems' carbon fluxes along a precipitation gradient. Philos. Trans. R. Soc. B Biol. Sci. 375:20190519. doi:10.1098/rstb.2019.0519.

Emanuel, K. 2021. Atlantic tropical cyclones downscaled from climate reanalyses show increasing activity over past 150 years. Nat. Commun. 12:7027. doi:10.1038/s41467-021-27364-8.

Fan, X., C. Miao, Q. Duan, et al. 2021. Future Climate Change Hotspots Under Different 21st Century Warming Scenarios. Earths Future 9. doi:10.1029/2021EF002027.

Friedlingstein, P., M.W. Jones, M. O'Sullivan, et al. 2022. Global Carbon Budget 2021. Earth Syst. Sci. Data 14:1917–2005. doi:10.5194/essd-14-1917-2022.

Fu, Z., P. Ciais, A.F. Feldman, et al. 2022. Critical soil moisture thresholds of plant water stress in terrestrial ecosystems. Sci. Adv. 8:eabq7827. doi:10.1126/sciadv.abq7827.

Gao, Y., J. Jia, Y. Lu, et al. 2021. Determining dominating control mechanisms of inland water carbon cycling processes and associated gross primary productivity on regional and global scales. Earth-Sci. Rev. 213:103497. doi:10.1016/j.earscirev.2020.103497.

Gentine, P., J.K. Green, M. Guérin, et al. 2019. Coupling between the terrestrial carbon and water cycles—a review. Environ. Res. Lett. 14:083003. doi:10.1088/1748-9326/ab22d6.

Gong, H., Y. Pan, L. Zheng, et al. 2018. Long-term groundwater storage changes and land subsidence development in the North China Plain (1971–2015). Hydrogeol. J. 26:1417–1427. doi:10.1007/s10040-018-1768-4.

Good, P., R. Chadwick, C.E. Holloway, et al. 2021. High sensitivity of tropical precipitation to local sea surface temperature. Nature 589:408–414. doi:10.1038/s41586-020-2887-3.

de Graaff, M.-A., J.D. Jastrow, S. Gillette, et al. 2014. Differential priming of soil carbon driven by soil depth and root impacts on carbon availability. Soil Biol. Biochem. 69:147–156. doi:10.1016/j.soilbio.2013.10.047.

Green, J.K., J. Berry, P. Ciais, et al. 2020. Amazon rainforest photosynthesis increases in response to atmospheric dryness. Sci. Adv. 6:eabb7232. doi:10.1126/sciadv.abb7232.

Green, J.K., S.I. Seneviratne, A.M. Berg, et al. 2019. Large influence of soil moisture on long-term terrestrial carbon uptake. Nature 565:476–479. doi:10.1038/s41586-018-0848-x.

Gu, L., J. Chen, J. Yin, et al. 2020. Projected increases in magnitude and socioeconomic exposure of global droughts in 1.5 and 2 °C warmer climates. Hydrol. Earth Syst. Sci. 24:451–472. doi:10.5194/hess-24-451-2020.

Hammond, W.M., A.P. Williams, J.T. Abatzoglou, et al. 2022. Global field observations of tree die-off reveal hotter-drought fingerprint for Earth's forests. Nat. Commun. 13:1761. doi:10.1038/s41467-022-29289-2.

Humphrey, V., J. Zscheischler, P. Ciais, et al. 2018. Sensitivity of atmospheric CO2 growth rate to observed changes in terrestrial water storage. Nature 560:628–631. doi:10.1038/s41586-018-0424-4.

Hussain, A., K.Z. Jadoon, K.U. Rahman, et al. 2022. Analyzing the impact of drought on agriculture: evidence from Pakistan using standardized precipitation evapotranspiration index. Nat. Hazards. doi:10.1007/s11069-022-05559-6.

Ichii, K., H. Hashimoto, M.A. White, et al. 2007. Constraining rooting depths in tropical rainforests using satellite data and ecosystem modeling for accurate simulation of gross primary production seasonality. Glob. Change Biol. 13:67–77. doi:10.1111/j.1365-2486.2006.01277.x.

Jensen, L., A. Eicker, H. Dobslaw, et al. 2019. Long-Term Wetting and Drying Trends in Land Water Storage Derived From GRACE and CMIP5 Models. J. Geophys. Res. Atmospheres 124:9808–9823. doi:10.1029/2018JD029989.

Jha, S., and R. Srivastava. 2018. Impact of drought on vegetation carbon storage in arid and semi-arid regions. Remote Sens. Appl. Soc. Environ. 11:22–29. doi:10.1016/j.rsase.2018.04.013.

Jing, W., L. Di, X. Zhao, et al. 2020. A data-driven approach to generate past GRACE-like terrestrial water storage solution by calibrating the land surface model simulations. Adv. Water Resour. 143:103683. doi:10.1016/j.advwatres.2020.103683.

Koutsoyiannis, D. 2012. Clausius–Clapeyron equation and saturation vapour pressure: simple theory reconciled with practice. Eur. J. Phys. 33:295. doi:10.1088/0143-0807/33/2/295.

Laloyaux, P., E. de Boisseson, M. Balmaseda, et al. 2018. CERA-20C: A Coupled Reanalysis of the Twentieth Century. J. Adv. Model. Earth Syst. 10:1172–1195. doi:10.1029/2018MS001273.

Landerer, F.W., F.M. Flechtner, H. Save, et al. 2020. Extending the Global Mass Change Data Record: GRACE Follow-On Instrument and Science Data Performance. Geophys. Res. Lett. 47:e2020GL088306. doi:10.1029/2020GL088306.

Landerer, F.W., and S.C. Swenson. 2012. Accuracy of scaled GRACE terrestrial water storage estimates. Water Resour. Res. 48. doi:10.1029/2011WR011453.

Lange, S., C. Menz, S. Gleixner, et al. 2021. WFDE5 over land merged with ERA5 over the ocean (W5E5 v2.0). doi:10.48364/ISIMIP.342217.

Li, X., Y. Li, A. Chen, et al. 2019. The impact of the 2009/2010 drought on vegetation growth and terrestrial carbon balance in Southwest China. Agric. For. Meteorol. 269–270:239–248. doi:10.1016/j.agrformet.2019.01.036.

Li, Y., Y. Xu, W. Zhang, et al. 2021. Carbon and water fluxes are more sensitive to drought than heat in terrestrial ecosystems in China. J. Hydrol. 603:127177. doi:10.1016/j.jhydrol.2021.127177.

Loomis, B.D., S.B. Luthcke, and T.J. Sabaka. 2019. Regularization and error characterization of GRACE mascons. J. Geod. 93:1381–1398. doi:10.1007/s00190-019-01252-y.

McDowell, N.G., G. Sapes, A. Pivovaroff, et al. 2022. Mechanisms of woody-plant mortality under rising drought, CO2 and vapour pressure deficit. Nat. Rev. Earth Environ. 3:294–308. doi:10.1038/s43017-022-00272-1.

Mercado, L.M., N. Bellouin, S. Sitch, et al. 2009. Impact of changes in diffuse radiation on the global land carbon sink. Nature 458:1014–1017. doi:10.1038/nature07949.

Nemani, R.R., C.D. Keeling, H. Hashimoto, et al. 2003. Climate-Driven Increases in Global Terrestrial Net Primary Production from 1982 to 1999. Science 300:1560–1563. doi:10.1126/science.1082750.

Ogunrinde, A.T., P.G. Oguntunde, A.S. Akinwumiju, et al. 2023. Effects of climate change and drought attributes in Nigeria based on RCP 8.5 climate scenario. Phys. Chem. Earth Parts ABC 129:103339. doi:10.1016/j.pce.2022.103339.

Oh, H., H.J. Kim, M.S. Mehboob, et al. 2023. Sources and uncertainties of future global drought risk with ISIMIP2b climate scenarios and socioeconomic indicators. Sci. Total Environ. 859:160371. doi:10.1016/j.scitotenv.2022.160371.

Pachauri, R.K., M.R. Allen, V.R. Barros, et al. 2014. Climate Change 2014: Synthesis Report. Contribution of Working Groups I, II and III to the Fifth Assessment Report of the Intergovernmental Panel on Climate Change. R.K. Pachauri and L. Meyer, ed. IPCC, Geneva, Switzerland.

Padiyedath Gopalan, S., A. Champathong, T. Sukhapunnaphan, et al. 2022. Inclusion of flood diversion canal operation in the H08 hydrological model with a case study from the Chao Phraya River basin: model development and validation. Hydrol. Earth Syst. Sci. 26:2541–2560. doi:10.5194/hess-26-2541-2022.

Pastorello, G., C. Trotta, E. Canfora, et al. 2020. The FLUXNET2015 dataset and the ONEFlux processing pipeline for eddy covariance data. Sci. Data 7:225. doi:10.1038/s41597-020-0534-3.

Pokhrel, Y., F. Felfelani, Y. Satoh, et al. 2021. Global terrestrial water storage and drought severity under climate change. Nat. Clim. Change 11:226–233. doi:10.1038/s41558-020-00972-w.

Pokhrel, Y.N., Y. Fan, and G. Miguez-Macho. 2014. Potential hydrologic changes in the Amazon by the end of the 21st century and the groundwater buffer. Environ. Res. Lett. 9:084004. doi:10.1088/1748-9326/9/8/084004.

Reichstein, M., E. Falge, D. Baldocchi, et al. 2005. On the separation of net ecosystem exchange into assimilation and ecosystem respiration: review and improved algorithm. Glob. Change Biol. 11:1424–1439. doi:10.1111/j.1365-2486.2005.001002.x.

Rodell, M., J.S. Famiglietti, D.N. Wiese, et al. 2018. Emerging trends in global freshwater availability. Nature 557:651–659. doi:10.1038/s41586-018-0123-1.

Ruehr, N.K., R. Grote, S. Mayr, et al. 2019. Beyond the extreme: recovery of carbon and water relations in woody plants following heat and drought stress. Tree Physiol. 39:1285–1299. doi:10.1093/treephys/tpz032.

Satish Kumar, K., E. Venkata Rathnam, and V. Sridhar. 2021. Tracking seasonal and monthly drought with GRACE-based terrestrial water storage assessments over major river basins in South India. Sci. Total Environ. 763:142994. doi:10.1016/j.scitotenv.2020.142994.

Save, H., S. Bettadpur, and B.D. Tapley. 2016. High-resolution CSR GRACE RL05 mascons. J. Geophys. Res. Solid Earth 121:7547–7569. doi:10.1002/2016JB013007.

Schwalm, C.R., W.R.L. Anderegg, A.M. Michalak, et al. 2017. Global patterns of drought recovery. Nature 548:202–205. doi:10.1038/nature23021.

Simmons, A.J., A. Untch, C. Jakob, et al. 1999. Stratospheric water vapour and tropical tropopause temperatures in Ecmwf analyses and multi-year simulations. Q. J. R. Meteorol. Soc. 125:353–386. doi:10.1002/qj.49712555318.

Sinha, D., T.H. Syed, and J.T. Reager. 2019. Utilizing combined deviations of precipitation and GRACE-based terrestrial water storage as a metric for drought characterization: A case study over major Indian river basins. J. Hydrol. 572:294–307. doi:10.1016/j.jhydrol.2019.02.053.

Slivinski, L.C., G.P. Compo, J.S. Whitaker, et al. 2019. Towards a more reliable historical reanalysis: Improvements for version 3 of the Twentieth Century Reanalysis system. Q. J. R. Meteorol. Soc. 145:2876–2908. doi:10.1002/qj.3598.

Stampfli, A., J.M.G. Bloor, M. Fischer, et al. 2018. High land-use intensity exacerbates shifts in grassland vegetation composition after severe experimental drought. Glob. Change Biol. 24:2021–2034. doi:10.1111/gcb.14046.

Sui, Y., X. Lang, and D. Jiang. 2018. Projected signals in climate extremes over China associated with a 2 °C global warming under two RCP scenarios. Int. J. Climatol. 38:e678–e697. doi:10.1002/joc.5399.

Syed, T.H., J.S. Famiglietti, M. Rodell, et al. 2008. Analysis of terrestrial water storage changes from GRACE and GLDAS. Water Resour. Res. 44. doi:10.1029/2006WR005779.

Teskey, R., T. Wertin, I. Bauweraerts, et al. 2015. Responses of tree species to heat waves and extreme heat events. Plant Cell Environ. 38:1699–1712. doi:10.1111/pce.12417.

Wan, J.-Z., C.-J. Wang, H. Qu, et al. 2018. Vulnerability of forest vegetation to anthropogenic climate change in China. Sci. Total Environ. 621:1633–1641. doi:10.1016/j.scitotenv.2017.10.065.

Wang, H.-M., J. Chen, C.-Y. Xu, et al. 2020a. A Framework to Quantify the Uncertainty Contribution of GCMs Over Multiple Sources in Hydrological Impacts of Climate Change. Earths Future 8:e2020EF001602. doi:10.1029/2020EF001602.

Wang, X., C. Zhao, C. Müller, et al. 2020b. Emergent constraint on crop yield response to warmer temperature from field experiments. Nat. Sustain. 3:908–916. doi:10.1038/s41893-020-0569-7.

Wolf, S., W. Eugster, C. Ammann, et al. 2013. Contrasting response of grassland versus forest carbon and water fluxes to spring drought in Switzerland. Environ. Res. Lett. 8:035007. doi:10.1088/1748-9326/8/3/035007.

Xi, X., and X. Yuan. 2022. Significant water stress on gross primary productivity during flash droughts with hot conditions. Agric. For. Meteorol. 324:109100. doi:10.1016/j.agrformet.2022.109100.

Xu, B., M.A. Arain, T.A. Black, et al. 2020. Seasonal variability of forest sensitivity to heat and drought stresses: A synthesis based on carbon fluxes from North American forest ecosystems. Glob. Change Biol. 26:901–918. doi:10.1111/gcb.14843.

Yang, Y, Yin, J, Guo, S, et al. Projection of terrestrial drought evolution and its eco-hydrological effects in China[J]. Science Bulletin, 2022. 10.1360/TB-2022-0566.

Yevjevich, V. 1969. An objective approach to definitions and investigations of continental hydrologic droughts. J. Hydrol. 7:353. doi:10.1016/0022-1694(69)90110-3.

Yin, J., P. Gentine, L. Slater, et al. 2023. Future socio-ecosystem productivity threatened by compound drought–heatwave events. Nat. Sustain. 1–14. doi:10.1038/s41893-022-01024-1.

Yin, J., P. Gentine, S. Zhou, et al. 2018. Large increase in global storm runoff extremes driven by climate and anthropogenic changes. Nat. Commun. 9:4389. doi:10.1038/s41467-018-06765-2.

Yin J., Guo S., Gu L., et al. 2021. Thermodynamic response of precipitation extremes to climate change and its impacts on floods over China. Chin. Sci. Bull. 66:4315–4325. doi:10.1360/TB-2021-0438.

Yin, J., S. Guo, Y. Yang, et al. 2022a. Projection of droughts and their socioeconomic exposures based on terrestrial water storage anomaly over China. Sci. China Earth Sci. 65:1772–1787. doi:10.1007/s11430-021-9927-x.

Yin, J., L. Slater, L. Gu, et al. 2022b. Global Increases in Lethal Compound Heat Stress: Hydrological

Drought Hazards Under Climate Change. Geophys. Res. Lett. 49:e2022GL100880. doi:10.1029/2022GL100880.

Yoshida, T., N. Hanasaki, K. Nishina, et al. 2022. Inference of Parameters for a Global Hydrological Model: Identifiability and Predictive Uncertainties of Climate-Based Parameters. Water Resour. Res. 58:e2021WR030660. doi:10.1029/2021WR030660.

Yu, G.-R., X.-F. Wen, X.-M. Sun, et al. 2006. Overview of ChinaFLUX and evaluation of its eddy covariance measurement. Agric. For. Meteorol. 137:125–137. doi:10.1016/j.agrformet.2006.02.011.

Yuan, W., W. Cai, A.L. Nguy-Robertson, et al. 2015. Uncertainty in simulating gross primary production of cropland ecosystem from satellite-based models. Agric. For. Meteorol. 207:48–57. doi:10.1016/j.agrformet.2015.03.016.

Zhang, L., J. Xiao, Y. Zheng, et al. 2020. Increased carbon uptake and water use efficiency in global semi-arid ecosystems. Environ. Res. Lett. 15:034022. doi:10.1088/1748-9326/ab68ec.

Zhang, Y., J. Joiner, S.H. Alemohammad, et al. 2018. A global spatially contiguous solar-induced fluorescence (CSIF) dataset using neural networks. Biogeosciences 15:5779–5800. doi:10.5194/bg-15-5779-2018.

Zhang, Y., T.F. Keenan, and S. Zhou. 2021. Exacerbated drought impacts on global ecosystems due to structural overshoot. Nat. Ecol. Evol. 5:1490–1498. doi:10.1038/s41559-021-01551-8.

Zhang, Y., X. Xiao, X. Wu, et al. 2017. A global moderate resolution dataset of gross primary production of vegetation for 2000–2016. Sci. Data 4:170165. doi:10.1038/sdata.2017.165.

Zhao, L., W. Huang, J. Chen, et al. 2020. Land use/cover changes in the Oriental migratory locust area of China: Implications for ecological control and monitoring of locust area. Agric. Ecosyst. Environ. 303:107110. doi:10.1016/j.agee.2020.107110.

Zhao, L., X. Wu, Z. Wang, et al. 2018. Soil organic carbon and total nitrogen pools in permafrost zones of the Qinghai-Tibetan Plateau. Sci. Rep. 8:3656. doi:10.1038/s41598-018-22024-2.

Zhao, M., G. A, I. Velicogna, et al. 2017. Satellite Observations of Regional Drought Severity in the Continental United States Using GRACE-Based Terrestrial Water Storage Changes. J. Clim. 30:6297–6308. doi:10.1175/JCLI-D-16-0458.1.

Zhao, M., G. A, J. Zhang, et al. 2021. Ecological restoration impact on total terrestrial water storage. Nat. Sustain. 4:56–62. doi:10.1038/s41893-020-00600-7.

Zheng, H., F.H.S. Chiew, S. Charles, et al. 2018. Future climate and runoff projections across South Asia from CMIP5 global climate models and hydrological modelling. J. Hydrol. Reg. Stud. 18:92–109. doi:10.1016/j.ejrh.2018.06.004.

Zhou, S., A.P. Williams, A.M. Berg, et al. 2019a. Land–atmosphere feedbacks exacerbate concurrent soil drought and atmospheric aridity. Proc. Natl. Acad. Sci. 116:18848–18853. doi:10.1073/pnas.1904955116.

Zhou, S., Y. Zhang, A. Park Williams, et al. 2019b. Projected increases in intensity, frequency, and terrestrial carbon costs of compound drought and aridity events. Sci. Adv. 5:eaau5740. doi:10.1126/sciadv.aau5740.

Zscheischler, J., M.D. Mahecha, J. von Buttlar, et al. 2014. A few extreme events dominate global interannual variability in gross primary production. Environ. Res. Lett. 9:035001. doi:10.1088/1748-9326/9/3/035001.